國　立　清　華　大　學

物理系碩士學位論文

鉛薄膜在鍺(001)表面的量子井態之角解析光電子能譜研究

Study of quantum well subband dispersions of Pb films on Ge(001) by Angle-resolved Photoemission(ARPES)

指導教授：唐述中教授　(Shu-Jung Tang)

研究生：陳珮文　(Pei-Wen Chen)

學號：9722507

中華民國九十九年七月

鉛薄膜在鍺（００１）表面的量子井能態之光電子能譜研究

國立清華大學物理研究所碩士學位論文

題目：鉛薄膜在鍺（００１）表面的量子井能態之光電子能譜研究

學生：陳珮文　　指導教授：唐述中

摘要

我們在新竹的國家同步輻射中心成功的在鍺（001）鉛重構（ c(4x8) phase ）的基底上製備平坦的鉛薄膜並且利用高解析度的角解析光電子能譜觀察隨層數變化的量子井能態，並記錄下４到１１層鉛薄膜的電子動能隨角度變化的二維影像進而得到佔有電子態在倒空間中的能譜。並以 Bohr-Sommerfeld rule 決定在鍺(001)基底對應Γ位置確切的量子井能態位置，根據這些能態位置得到對應的倒空間位置去計算模擬每一層數的量子井能態分佈。我們將計算的能帶與測量得到的能譜做比較，發現除了在布理淵區(Brillouin Zone)中心的範圍，其它部分非常吻合。受到鍺基底價電帶邊緣與鉛薄膜電子態的相互作用下，在價電帶邊緣之下的量子井能態分佈會受到影響，在價電帶邊緣產生扭結（kink）。更進一步我們發現，當鉛薄膜量子井能態經過重電洞價電帶邊緣（Heavy hole band edge）時並不受到影響，但在輕電洞價電帶邊緣（Light hole band edge）和自旋軌道分裂價電帶邊緣（Split-off band edge）附近，我們可以看到類似扭結的現象使得量子井能帶分佈扭曲。這些結果可以用安德森模型（Anderson Model）去解釋，也藉由檢視鉛薄膜量子井能態與鍺基底價電子能態的軌道對稱性，可以去解釋重電洞價電帶為何與鉛薄膜量子井能帶沒有作用。我們也從測到的電子能譜中發現，奇數層能譜中對應到的量子井能帶只有它自己本身層數，而偶數層能譜可以看到除了它自己本身層數以外還有上下兩層的量子井能帶存在。這表示著偶數層是一個比較不穩定的層數。另外，這個結果也跟我們做的熱穩定實驗結果十分一致。

Study of quantum well subband dispersions of Pb films on Ge(001) by Angle-resolved Photoemission Spectroscopy(ARPES)

Student：Pei-Wen Chen　Advisors：Dr. Shu-Jung Tang

Master Degree in Physics, National Tsing Hua University

Abstract

In our work, atomically uniform Pb films were prepared on Pb/Ge(001)-c(4X8) reconstructed surface at the thickness ranging 4~16 ML. The measurement of Quantum well subbands of the thickness dependence of the in-plane band dispersions for Pb films on Ge(001) was performed and the peak positions of quantum well states(QWS) at normal emission were determined by Bohr-Sommerfeld quantization rule. According to these discrete peak positions of QWSs, we calculate the Pb subbands to simulate the quantum well states by using Tihght-binding approximation. It is interesting that the calculated and measured results matched each other except for the region near the zone center. The deviation is due to the interaction between QWS subbands and Ge band edges. Moreever, we found heavy hole(HH) band edge crossed the QWS subbands without causing interaction.In contrast, Light hole(LH) and split-off hole(SO) band edges caused the distortion of QWS subbands, which shows a break(kink) at the crossover point. This phenomenon can be described well by hybridization interaction based on many-body Anderson Model and the symmetry argument regarding explain why the QWS subbands don't interact with Ge HH band edge by examing the orbital symmetries of Pb QWS and Ge band edges, as we observed. By examing the QWS subband dispersions, we found the QWS peaks became sharper at off-normal position above the LH band edge. For most of odd layers, only the subbands corresponding to N layers exist, but for even

layers, both subbands, corresponding to N-1 and N+1 layers coexist. This indicates that there are three thicknesses (N-1, N, N+1) coexisting for even layers and the films of even layers should be unstable. This result is also consistent with that from the thermal stability measurement. Consequently, the layer resolution of Pb films were revealed via the observed splitting of the subbands within the region.

Acknowledgement

感謝我的指導老師唐述中教授兩年來的教導讓我學到對研究的堅持及態度，唐老師很有耐心的指導我，讓我可以更深入了解實驗數據中所帶有的物理意義與現象；感謝同步輻射中心的鄭澄懋博士對於實驗上以及生活上的援助讓我得到許多實用的知識和經驗，還要謝謝蘇雲良老師對於論文的指導使我的成果能夠呈現的更美好；謝謝心誼、文凱、鈺梅、建中、昌燁和彥豪學長姐留下來的經驗以及在離開實驗室後仍然願意給予我們幫助和建議。

謝謝宇軒和我一起努力奮鬥並且在我需要修課時承擔實驗的辛苦，在實驗時也總是給予信心和歡樂，在對實驗的理解與想法上，從你這邊我也學到很多，都讓我覺得很佩服！謝謝棋斌跟哲嘉總是在實驗或是數據分析上給予我一些建議，在我陷入實驗數據困境中拉我一把，給予一些很有用的建議與意見。謝謝仲桓、立言和慶鴻幫我們一起做實驗並且帶來歡樂，一起熬過了實驗的艱困期，讓我們不至於體力透支。謝謝實驗室的大家，我大概永遠不會忘記這一年，很特別的跟你們一起在實驗室度過了聖誕節和跨年。還有謝謝可芳、嘉仁常常幫我們買便當，另外也謝謝在我們實驗遇到困難時，總是不吝伸出援手幫助我們解決問題的同步輻射中心研究員們。

最後，要感謝我的家人們和簡瑋總是給予我支持，在我難過沮喪的時候可以找到重新站起來的力量；也感謝清大諮商中心可愛的老師與義工們，常常帶給我溫暖與歡笑，讓我這兩年的碩士生涯感到不孤單。也謝謝這兩年來曾經關心過我與幫助我的朋友們，有你們的支持與鼓勵是我最美好的回憶。

Contents

Chapter 1

Introduction

Ultrathin metal films play an increasingly important role in many technologies and are the subject of intense scientific research. The electronic properties of metallic thin films grown on substrates deviate from those of the metal bulk, and the phenomenon is frequently termed as quantum size effect (QSE). Recently, there have been many experiments reporting that atomic flat metallic thin films can grow on semiconductor substrate, including Ag/Si(111) [18], Pb/Ge(111) [19], Pb/Si(111) [20]...etc. Recent experiments show the quantum size effect in these atomically flat films has strong influence on other properties of these films, such as superconducting[23], electron-phonon coupling[24] and lattice relaxation[25]. This means that one can control the film properties by adjusting the film thickness.

As the film thickness is reduced to the order of an electron wavelengt, the wave vectors of the electrons in the normal directions of the film are quantizied, and the corresponding discrete electronic states are the well-known quantum well states (QWS). The discrete energy levels of the QWS greatly modulate the density of states

of the electrons near the Fermi level(E_F), and thus significantly affect the physical and chemical properties of a system.

Angled-resolved photoemission spectroscopy(ARPES) is a powerful technology to probe the electronic structures of the solids. It's also surface sensitive, so we use ARPES to measure the energy band structures of the thin Pb/Ge(001), based on which, we can derive some physical properties in the thin film system.

In the following chapter, the background knowledge of photoemission spectroscopy is introduced in Chapter 2. Then, Chapter 3 describes the basic concepts of the surface system. The investigation of electronic structures for Pb/Ge(001) system by ARPES is described in Chapter 4. The interaction between the Ge(001) substrate and the Pb thin films and its influence on the properties of Pb films are discussed. Finally, the results are summarized in Chapter 5.

Chapter 2

Photoemission

2.1 Introduction

Photoemission Spectroscopy(PES) is one of most important methods to study the electronic structure of solids and surfaces. Furthermore , PES has widespread practical implications in various fields such as surface chemistry and material science...etc, contributing to significant understanding of fundamental principles in solid state physics. The technique is based on the photoelectric effect first observed by Hertz and Wilhelm Hallwachs in 1887. Then Albert Einstein introduced a new concept of "photon" and explained the photoelectric effect by the Eq. (2.1) in 1905.

$$E_{kin}^{max} = h\nu - \Phi_0 \tag{2.1}$$

where $h\nu$ is the photon energy and Φ_0 is the work function of the sample surface.

A photoemission experiment involves a monochromatic photon beam impinging on sample and the emitted photoelectrons detected by an analyzer in Vacuum environment, as shown in Fig. 2.1. The photon source can be a gas discharge lamp or synchrotron radiation. Furthermore, the photon energy range may be in the ultra-

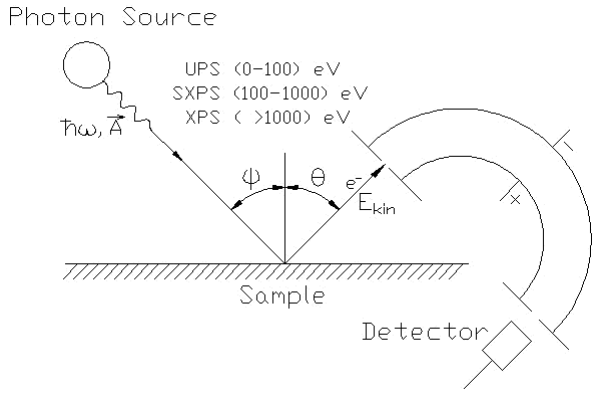

Figure 2.1: Sketch of a modern PES experiment.

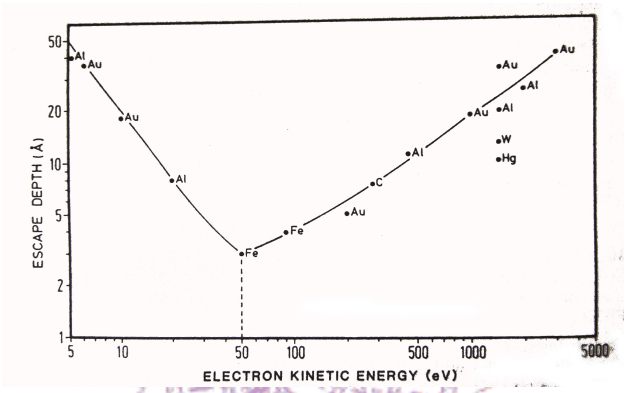

Figure 2.2: Mean free path (λ) as a function of electron kinetic energy for various material.

violet regime($5 \sim 100eV$, UPS), in the soft X-ray regime($100 \sim 1000eV$, SXPS) or in the X-ray regime($> 1000eV$, XPS).

Fig. 2.2 shows mean free path (λ) as a function of electron kinetic energy for different materials as seen, electrons with kinetic energy $20 \sim 100$ eV corresponding to a short mean free path are ideal to probes for the surface.

2.2 The Photoemission Process

The Photoemission Process can be illustrated as Fig. 2.3. An electron beam with energy $\hbar\omega$ is incident on the sample. As a result , electrons are emitted by photoelectric effect and escape in vacuum with kinetic energy in all directions. And

the kinetic energies of photoelectrons can be derived from energy conservation as

$$\hbar\omega = E_f - E_i$$

$$E_i = -|E_B|, E_f = E_{kin} + \Phi$$

where $\hbar\omega$ is the incident photon energy , E_i is initial energy, E_f is final energy, Φ is work function and $|E_B|$ is the binding energy which equals to the energy separation between Fermi Level and initial energy $|E_F - E_i|$. Then, we can derive the Eq. (2.2).

$$E_{kin} = \hbar\omega - \Phi - |E_B| \tag{2.2}$$

Besides, there are some rigorous theoretical approaches to the photoemission process. These theoretical approaches require a full quantum-mechanical treatment of the complete coherent process in which an electron is removed from an occupied state within the solid and detected by analyzer. However, the most commonly used method is three-step model, which will be introduced in the following page.

2.2.1 Three-step Model

The three-step model is a purely phenomenological approach which subdivides the photoemission process into three independent and sequential steps , as shown in Fig 2.4 [6] :

1. Optical excitation of an electron from an initial to a final state within the crystal.

2. Propagation of the excited electron.

3. Emission of the electron from the solid into vacuum.

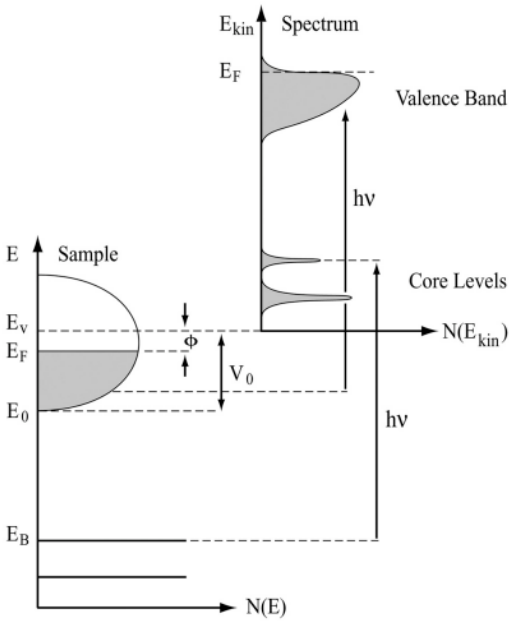

Figure 2.3: Energetics of the photoemission process. The electron energy distribution result from incoming photons and measured as a function of the kinetic energy of the photoelectron [6].

The total photoemission intensity is then given by the product of three independent terms : the total probability for the optical transition, the scattering probability for the traveling electrons and the transmission probability through the surface potential barrier.

Step 1 : Optical excitation of the electron in the solid.

Neglecting the momentum of the photon that is much smaller than the typical reciprocal lattice of a solid, the optical transition is a direct transition in the reduced zone scheme. The transition probability between the N-electron ground state Ψ_i^N and one of possible final state Ψ_f^N can be approximated by Fermi Golden Rule such as :

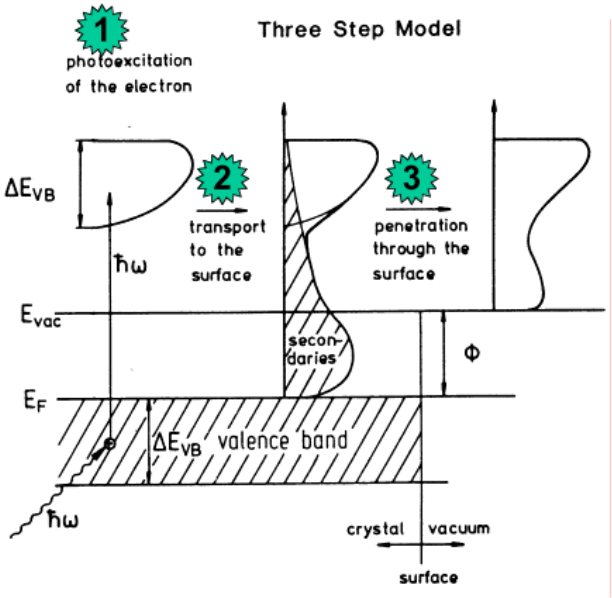

Figure 2.4: Illustration of the three-step model in PES. The three-step model consists of (1) photoexcitation of an electron, (2) transport to the surface and (3) transmission through the surface into the vacuum [6].

$$\omega_{fi} = \frac{2\pi}{\hbar}| < \Psi_f^N|H_{int}|\Psi_i^N > |^2\delta(E_f^N - E_i^N - \hbar\omega) \tag{2.3}$$

where E_f^N and E_i^N are the final and initial-state energies of the N-particle system. The interaction with the photon is treated as a perturbation given by :

$$H_{int} = \frac{e}{2m_e c}(\mathbf{A}\cdot\mathbf{p} + \mathbf{p}\cdot\mathbf{A}) \cong \frac{e}{mc}\mathbf{A}\cdot\mathbf{p} \tag{2.4}$$

$\mathbf{A}$ is the vector potential of incident electromagnetic waves and $\mathbf{p}$ is the momentum operator of the electron. And it would be convenient to factorized the wavefunction in Eq. (2.3) into photoelectron and (N-1)-electron system. Assume an electron is instantaneously removed and the effective potential of the system changes discontinuously at that instant. The final state Ψ_f^N and initial state Ψ_i^N can be written as

$$\Psi_f^N = A\Phi_f^k\Psi_f^{N-1}; \Psi_i^N = A\Phi_i^k\Psi_i^{N-1}$$

where A is an antisymmetric operator that properly antisymmetrizes N-electron wavefunction so that the Pauli principle is satisfied. Φ_f^k is the wavefunction of the photoelectron with momentum k, and Ψ_f^{N-1} is the final state wavefunction of the (N-1)-electron system left behind. Φ_i^k is on-electron orbital. So the matrix element in Eq. (2.3) can be written as

$$< \Psi_f^N|H_{int}|\Psi_i^N > = < \Phi_f^k|H_{int}|\Phi_i^k >< \Psi_m^{N-1}|\Psi_i^{N-1} > \tag{2.5}$$

where $< \Phi_f^k|H_{int}|\Phi_i^k > \equiv M_{f,i}^k$ is the one-electron dipole matrix element and the second term is the (N-1)-electron overlap integral. The total photoemission intensity measured as a function of E_{kin} at a momentum k, namely $I(k, E_{kin}) \equiv \sum_{f,i}\omega_{f,i}$ is then proportional to :

$$N_{int}(E_{kin}, \hbar\omega) = \sum_{f.i} |M^k_{f,i}|^2 \sum_m |c_{m,i}|^2 \delta(E_{kin} + E^{N-1}_m - E^N_i - \hbar\omega) \tag{2.6}$$

where $|c_{m,i}|^2 = | < \Psi^{N-1}_m | \Psi^{N-1}_i > |^2$ is the probability that the removal of an electron from state i will leave the (N-1)-particle system in the excited state m.

Step 2 : Transport of the electron to the surface.

Photoexcited electrons may be scattered by phonons, plasmons or electrons and lose some kinetic energy during the propagation. These electrons are called secondary electrons and contribute to a continuous background in the spectra which is usually ignored or subtracted. The transport fraction of the total number of photoexcited electrons can be expressed by a coefficient $d(E, \mathbf{k})$

$$d(E, \mathbf{k}) \simeq \frac{\alpha\lambda}{1 + \alpha\lambda} \tag{2.7}$$

where α is the optical absorption of light and λ the mean free path of electron. The mean free path is the average distance between collisions of two photoexcited electrons. Knowing that λ is much smaller than α^{-1}, one obtains $d(E, \mathbf{k}) \rightarrow \alpha\lambda$ which indicates the transportation without inelastic collision is proportional to the mean free path.

Step 3 : Escape of the electron into vacuum.

The escaping electrons from surface have enough kinetic energy to overcome the potential barrier of the surface. And the other electrons are totally reflected back into the bulk. In any case, the 2D translational symmetry of surface is not broken during photoemission. So the transmission of the photoexcited electron penetrating

the surface into the vacuum requires conservation of its wave vector component parallel to the surface:

$$\mathbf{k}_{\parallel}^{ex} = \mathbf{k}_{\parallel}^{in} + \mathbf{G}_{\parallel}; \tag{2.8}$$

where $\mathbf{k}_{\parallel}^{ex}$ and $\mathbf{k}_{\parallel}^{in}$ are the wave vector of the excited electron outside and inside the crystal respectively, and $\mathbf{G}_{\parallel}$ is the surface reciprocal lattice vector. The normal component of the wave vector is not conserved because of broken translational symmetry along the direction perpendicular to the surface. But $\mathbf{k}_{\perp}^{ex}$ can be determined from energy conservation as below

$$E_{kin} = \frac{\hbar^2}{2m}[(\mathbf{k}_{\parallel}^{ex})^2 + (\mathbf{k}_{\perp}^{ex})^2] = E_f - E_{vac} \tag{2.9}$$

where E_f is the final energy and E_{vac} is the vacuum level.

So the transmission rate can be described as

$$T(E, \mathbf{k})\delta(\mathbf{k}_{\parallel} + \mathbf{G}_{\parallel} - \mathbf{k}_{\parallel}^{ex}). \tag{2.10}$$

Therefore, the formula for the external emission current in the three-step model writes

$$I_{int}(E, \hbar w, \mathbf{k}_{\parallel}^{ex}) \propto N_{int}(E, \hbar w) d(E, \mathbf{k}) T(E, \mathbf{k}) \delta(\mathbf{k}_{\parallel} + \mathbf{G}_{\parallel} - \mathbf{k}_{\parallel}^{ex}) \tag{2.11}$$

2.3 Angle-Resolved Photoemission Spectroscopy(ARPES)

Angle-Resolved Photoemission adds a new dimension to photoelectron spectroscopy. The intensity and energy dependence can be measured as a function of the emission angle with respect to the fixed axes. The emission angle Θ is defined

as shown in Fig. 2.1. However, what we concerned is the electronic dispersion $E_{\mathbf{k}}$ vs the total crystal wave vector $\mathbf{k}$, so there are some relationship between the wave vector and emission angle to deduce the electronic dispersion relations $E_{\mathbf{k}}$ for the solid. The wave vector or the momentum $\mathbf{k} = \mathbf{p}/\hbar$ of photoelectrons with kinetic energies E_{kin} in vacuum is given by $\mathbf{k}^{ex} = \sqrt{2mE_{kin}}/\hbar$. Because of the translational symmetry across the surface plane parallel to the sample surface , the parallel component of the electron momentum ($\mathbf{k}_{\parallel}^{ex}$), which is conserved in the process, can be written as

$$\mathbf{k}_{\parallel}^{in} = \mathbf{k}_{\parallel}^{ex} + \mathbf{G}$$

where $\mathbf{k}_{\parallel}^{ex}$ is the component parallel to the sample surface of the electron crystal momentum in the extended-zone scheme. Consider $\mathbf{G} = 0$ (no umklapp effect) for simplification, as shown in Fig. 2.5.

$$\mathbf{k}_{\parallel}^{in} = \mathbf{k}_{\parallel}^{ex} = \sqrt{\frac{2mE_{kin}}{\hbar^2}} \sin\Theta \tag{2.12}$$

Further, the wave vector $\mathbf{k}_{\perp}^{ex}$ normal to the surface, which is not conserved, can be determined by some assumption made for the dispersion of the electron final state involved in the photoemission process. Assume a free-electron final state band, and one can obtain from Eq.(2.12) and $E_f = E_{kin} + \phi$

$$\mathbf{k}_{\perp}^{ex} = \sqrt{\frac{2mE_{kin}}{\hbar^2} \cos^2\Theta + V_0}$$

where ϕ is work function and V_0 is the inner potential that the sum of the work function ϕ and the Fermi energy E_F.

In our experiment, the energy analyzer and photon beam are at fixed position. In order to detect the photoelectrons emitted from surface in different angles for some

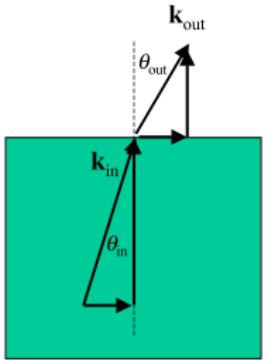

Figure 2.5: The schematics of photoelectrons momentum.

symmetric directions, the sample will be rotated by azimuthal angle. The definition of parameters in ARPES experiment ,as shown in Fig. 2.1, are incident angle φ and emission angle Θ. As φ is changed ,the angle between the surface and the light polarization is also changed. The intensity of peaks is proportional to the matrix element of the interaction operator which relates to the geometry of the polarization of light. The polarization of light affects the cross section, and the intensity of the detected state is also affected.

2.3.1 Symmetry of Initial States and Selection Rule

According to Eq.(2.6) the photoemission intensity is determined by the matrix elements of the form

$$< \Phi_f^k | \frac{e}{mc} \mathbf{A} \cdot \mathbf{p} | \Phi_i^k > \equiv M_{f,i}^k$$

where $\mathbf{A}$ is the vector potential of the incoming light and $\mathbf{p}$ is the momentum operator ($\mathbf{p} = \hbar\nabla/i$). We can observe particular initial states by considering special experimental geometries and the symmetry of the electronic states involved. Assume that there is a mirror plane in the surface, as shown in Fig. 2.6, and both

the direction of incidence of the exciting light and the detection direction for the emitted electrons are within the mirror plane. The initial states can be classified as being odd or even with respect to reflection in the mirror plane. The final state wave function must always be even, otherwise a detector located in the mirror plane would see a node of the emitted electrons. So the polarizations of the incoming light determine whether the initial state wave function would be detected or not. If the vector potential $\mathbf{A}_1$ is parallel to the mirror plane(yz), the momentum operator contains only components $\partial/\partial y$ and $\partial/\partial z$ that are even with respect to reflection in the mirror plane. If the vector potential $\mathbf{A}_2$ is perpendicular to the mirror plane, only $\partial/\partial x$ occurs in the perturbation operator. In order to detect the photoemission signal for both polarizations one requires :

for $\mathbf{A}_1 \| (yz)$:

$$< \Phi_f^k | \frac{\partial}{\partial y} | \Phi_i^k > \neq 0$$

$$< \Phi_f^k | \frac{\partial}{\partial z} | \Phi_i^k > \neq 0$$

with $< \Phi_f^k |$, $\frac{\partial}{\partial y}$, $\frac{\partial}{\partial z}$ and $|\Phi_i^k >$ even ;

for $\mathbf{A}_1 \perp (yz)$:

$$< \Phi_f^k | \frac{\partial}{\partial x} | \Phi_i^k > \neq 0$$

with $< \Phi_f^k |$ even and $\frac{\partial}{\partial x}$, $|\Phi_i^k >$ odd.

An appropriate choice of the experimental geometry can give important information about the symmetry character(s-, p- or d-like) of electronic surface state bands and also about molecular orbitals of adsorbates [1].

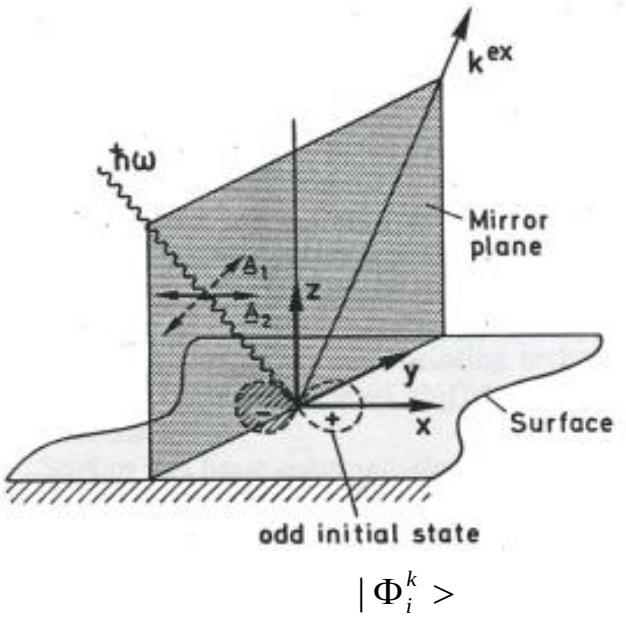

Figure 2.6: Symmetry selection rule in a photoemission experiment. The direction of the incident light($\hbar\omega$) and the trajectory of the emitted electron(wave vector $\mathbf{k}^{ex}$) lie in a mirror plane of the crystal surface.

2.4 Photoemission Spectra

From previous section, we have introduced the probability that the removal of an electron from state i will leave the (N-1)-particle system in the excited state m, expressed as $|c_{m,i}|^2 = | < \Psi_m^{N-1}|\Psi_i^{N-1} > |^2$. In the non-interacting limit, if $\Psi_i^{N-1} = \Psi_{m_0}^{N-1}$ for one particular $m = m_0$, the corresponding $|c_{m_0,i}|^2$ will be unity and all the others $|c_{m_0,i}|^2$ zero. So one can therefore write

$$A(\mathbf{k},\omega) = \delta(E_{kin} + E_m^{N-1} - E_i^N - \hbar\omega)$$

where $A(\mathbf{k},\omega)$ denotes the spectral function of the hole state for the case of a 2D electronic state, because the final state effect can be neglected.

In the strongly correlated systems, however, many of the $|c_{m_0,i}|^2$ will be different from zero because the removal of the photoelectron results in a strong change of the system effective potential and Ψ_i^{N-1} will have an overlap with many of the eigenstates $\Psi_{m_0}^{N-1}$. The spectral function provides information about the nature of the allowed electronic states, regardless whether they are occupied or not, and can be considered as a generalized density of states. Further, it can be expressed as the form of Lorenzian Function.

$$A(\mathbf{k},\omega) = \frac{1}{\pi}\frac{|Im\,(\Sigma(\mathbf{k},\omega))\,|}{[\omega - \epsilon_{\mathbf{k}} - Re\,(\Sigma(\mathbf{k},\omega))]^2 + [Im\,(\Sigma(\mathbf{k},\omega))]^2}. \tag{2.13}$$

where $\Sigma(\mathbf{k},\omega)$ is the hole self energy $\Sigma(\mathbf{k},\omega) = \Sigma'(\mathbf{k},\omega) + i\Sigma''(\mathbf{k},\omega)$. Its real part and imaginary part contain all the information on the energy renormalization and lifetime, respectively , of an hole with band energy $\epsilon_{\mathbf{k}}$ and momentum $\mathbf{k}$ propagating

in a many-body system. ARPES directly probes the spectral function $A(\mathbf{k}, \omega)$ of the occupied states. Not only the effect of the matrix element term has to be taken into account, but also the finite experimental resolution and extrinsic background due to secondary electrons. The latter effects may be expressed explicitly for photoelectron current as

$$\int d\omega' d\mathbf{k}' I_0(\mathbf{k}', \mathbf{A}) f(\omega') A(\mathbf{k}', \omega') R(\omega - \omega') Q(\mathbf{k} - \mathbf{k}') + B \tag{2.14}$$

where R and Q are the resolutions of energy and momentum, and B is a function of background. R and Q usually can be modeled as Gaussian function, and B can be modeled as a polynomial function in electron energy.

In ARPES experiment, The spectrums we collected are composed of energy distribution curves (EDC). The EDC describes the variation of photoelectron counts with kinetic energy collected at a specific photon energy and emission angle, as shown as Fig. 2.7. It mainly consists of three parts : occupied state peak, a sharp cutoff and background.

The occupied states, such as core level and valence states, exhibit as peaks in energy distribution curve. Core level states arise from electrons that are tightly bound to the nucleus and appear at smaller kinetic energy. Valence states arise from outermost electrons of an atom, which determine how the atom interacts with other atoms, and is mostly close to Fermi level.

The cutoff indicates where the Fermi level of the sample lies. But the cutoff is not always ideally sharp in spectra, it's affected by the finite temperature which causes a small number of counts populating the region above the Fermi level. When Fermi

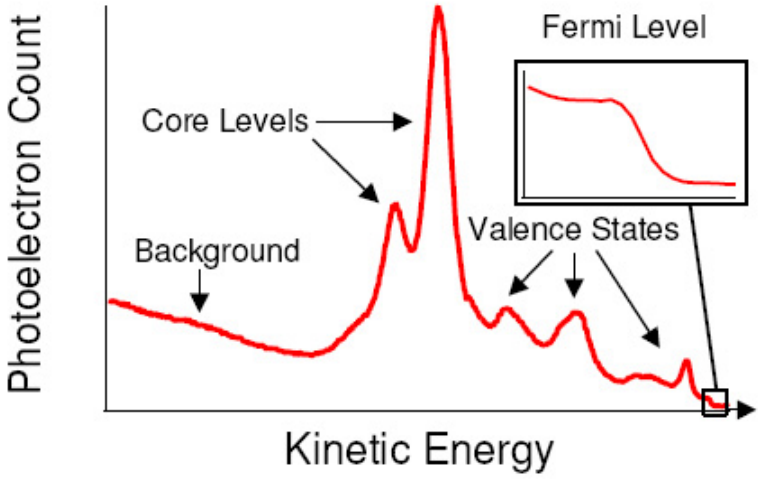

Figure 2.7: The schematic of the photoemission spectrum exhibits the typical features including background, Fermi level, and electron state peak.

level falls in an energy gap, there is no obvious cutoff in spectra.

2.5 Sources of Photons

Photoemission requires high intensity and monochromatic photon source. Photon sources for a PES experiment can be X-ray tube, laser system, gas-discharge lamps or synchrotron radiation sources. In our experiment, the photon sources are basically used by UV lamp and synchrotron radiation, which are introduced by the following section.

2.5.1 Helium Lamp

Gas-discharged lamps are used as light source for the UV range. The operation of the high intensity VUV Source HIS 13 lamp is based on the principle of a cold cathode capillary discharge. When the high voltage bias applied between the ends of an insulating tube filled with gas is large enough, spontaneous breaking through

Table 2.1: Positions and intensities of He cold cathode discharge lines.

Source	Energy [eV]	rel. Intensity
He I α	21.22	100
He I β	23.09	1.2
He I γ	23.74	0.5
He II α	40.81	100
He II β	48.37	< 10
He II γ	51.02	n.a.

occurs leading to a continuous discharge. The ignition voltage is larger than the operating one to maintain a continuous discharge.

In our experiment, the He gas is used to mainly provide two photon energies of 21.2 eV and 40.8 eV. The photon energy provided by He gas is shown as Table 2.1. The photon energy that we mostly used is 21.2 eV , because its intensity is much higher than others.

2.5.2 Synchrotron Radiation

Some data of our experiment were taken by using the lights from the beamlines at BL21B1 and BL03A1 in National Synchrotron Radiation Research Center (NSRRC). The BL21B beamline is an ultra-high resolution and high flux U9 cylindrical grating monochromator (U9-CGM) beamline, covering the photon energies from 5 to 100 eV. Two energy branches using separate entrance slits and incident angles are used to optimize the overall performance.[9] The BL03A1 HF-CGM high flux and

high resolution beamline covers photon energies from 4 to 40 eV. This beamline, which collects 50 mrad of the horizontal radiation, uses a six-meter cylindrical grating monochromator (6m-CGM) with an incident angle of 70 degree instead of the conventional normal incidence monochromator (NIM) design [9].

Synchrotron radiation is light emitted by the electrons undergoing centripetal acceleration according to Electromagnetic mechanics. Synchrotron facilities feature a storage ring where the charged particles are bent into a quasi-circular trajectory by magnetic fields. When electrons are accelerated to travel a nonlinear course, they emit electromagnetic radiation. Under non-relativistic conditions, the radiation will adhere to a dipole distribution around the electron. Whenever electrons moving close to the speed of light, $\beta \sim 1$, are deflected by a magnetic field, the radiation converges into a thin beam of radiation tangentially from their path due to Lorentz transformation (effect).

In NSRRC, the electrons are first accelerated in the linear accelerator (LINAC) that boosts the electrons up to an energy of 50 MeV, and the booster ring then accelerates the electrons to an energy of 1.5 GeV. The electrons traveling at 99.999995 percent of the speed of light are then guided through a 70-meter-long transport line and into the storage ring, where electrons with an energy of 1.5 GeV circulate in an ultra-high-vacuum chamber for several hours. A series of magnets situated around the ring steer the electrons along circular arcs, and synchrotron radiation is continuously emitted tangentially from the arcs. The emitted light is channeled by the insertion devices through beamlines to the experimental end stations where experiments are conducted [9].

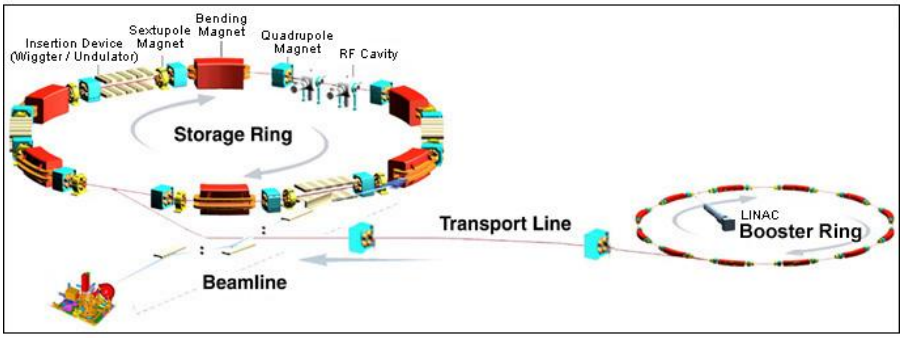

Figure 2.8: Storage ring and booster ring in NSRRC

Insertion devices (wigglers and undulators) comprising rows of magnets with alternating polarity produce brighter synchrotron radiation by causing the beam to oscillate rapidly. Wigglers cause multiple direction changes in the electron beam that generate extremely bright white light with short wavelengths; undulators cause periodic changes in the electron beam's direction that produce ultra-brilliant, single-wavelength radiation from the resulting interference patterns.

2.6 Energy Analyzer

The SCIENTA R3000 is equipped in our chamber. It's a high-resolution electron energy analyzer developed for photoelectron spectroscopy. The SCIENTA R3000

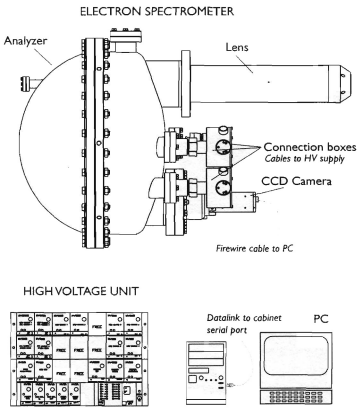

Figure 2.9: Schematic overview of the SCIENTA R3000 system parts.

system contains of three main parts, which is shown in Fig. 2.9

1. Input lens for receiving electrons.

2. Hemispherical analyzer for spectroscopic measurements.

3. Detector assembly with a CCD camera for signal detection.

An elaborate multi-element electrostatic lens acts as a focusing lens, which was used to collect and transfer electrons from the sample to the entrance slit of the hemispherical energy analyzer. It also matches the initial kinetic energy of the electrons to the fixed pass energy of the energy analyzer. That is

$$E_{pass} = E_{kin} - eV_{retarding}$$

where $V_{retarding}$ is the retarding potential provided by the electric lens to slow down the electron. By scanning the retarding potential one can effectively record the photoemission intensity versus the photoelectron kinetic energy. The pass energy is the kinetic energy of the electron at the center of the detected energy band when it passed through the hemispherical part of the analyzer.The pass energy relies on the voltage difference between the inner and outer spheres. The relationship can be

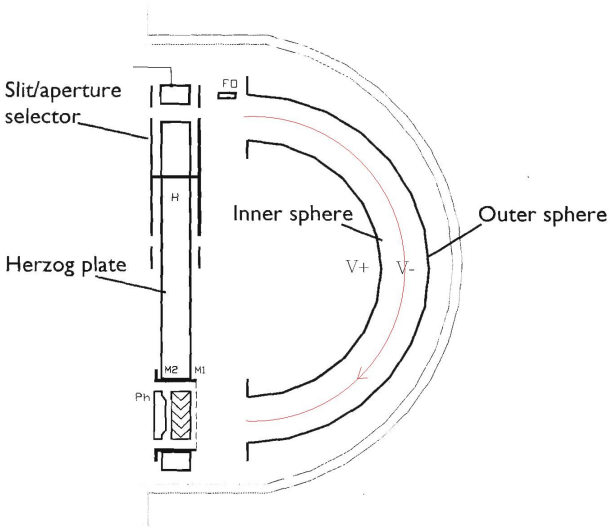

Figure 2.10: Schematic drawing of the SCIENTA R3000 analyzer

written as

$$E_{pass} = e(V_+ - V_-)(\frac{R_+R_-}{R_-^2 - R_+^2})$$

where $R_+(R_-)$ and $V_+(V_-)$ are the radius and voltage for inner(outer) sphere, as shown Fig. 2.10.

Electrons trajectories are bent in at 180° radial electrostatic field between the two hemispheres with a pass energy dependent voltage difference between them. The bending radius will depend on the initial electron kinetic energies ,which result in a distribution of electrons with respect to kinetic energies at the detector.

The end of radial electrostatic field is a field termination mesh in front of the detector system. The field termination mesh renders the negative bias used to repel the low-energy secondary electron. And the detector assembly consists of two Multi-Channel Plates(MCP) and a phosphorous screen. The MCP pair multiplies each incoming electron about a million times. This electron pulse is accelerated to the phosphorous screen producing a light flash detectable by the FireWire CCD camera. The detector area registered by the CCD camera is a square of over 600 simultaneous

energy channels and over 400 channels in the spatial or angular direction; that is, the MCP/CCD camera detection system is a 2-D detection system with energy in one direction and spatial or angular information in the other direction. And the spatial/angular dispersion is controlled by the choice of lens mode.

The lens mainly is operated in two lens modes : Transmission Mode and Angular Multiplexing Mode. The transmission mode is the standard method of lens operation. It produces an image of the sample on the detector and is intended for large-spot analysis of relatively homogeneous samples. The spatial resolution in Transmission Mode is in the order of $300\mu m$; Angular Mode is used for ARPES measurements, which efficiently probe the energy band structure of solids. The angular resolution will vary with the emission spot size, where small spot sizes give the highest resolution.

It's possible to modify the energy resolution and peak intensity by varying the analyzer entrance slit size and shape, and the pass energy. The theoretical energy resolution is approximated with

$$\Delta E \approx s \cdot E_{pass}/2r$$

where s is the slit width and r is the analyzer radius. With an MCP detector/CCD camera detection system the intensity scales approximately as $\sqrt{E_{pass}}$. As a rule of thumb high pass energy and large slit gives the best count rate. The SCIENTA R3000 system is equipped with six selectable slits, three curved and three straight slits as shown in Table 2.2. The photon beam also affects the electron energy resolution. Better energy resolution leads to lower intensity and maybe a small spot size. For Helium lamp, the photon energy resolution is fixed; but it's tunable by the beamline slits in synchrotron radiation light. Therefore, the total energy

Table 2.2: Six modes of slit [10].

Mode	Width (mm)	Length (mm)	Shape
1	0.2	20	Straight
2	0.2	20	Curved
3	0.4	20	Curved
4	0.8	20	Curved
5	1.3	20	Straight
6	3.0	20	Straight

resolution consists of two parts ,the energy resolutions of the energy analyzer and of the incident photon beam. It can be expressed as

$$\Delta E = \sqrt{\Delta E^2_{photons} + \Delta E^2_{analyzer}}. \tag{2.15}$$

The actual photoemission experiment is performed in the analyzer, not in the vacuum. The kinetic energies E measured in vacuum and E_{kin} measured in an analyzer are not equivalent because the work functions of sample and analyzer are different. The sample and the analyzer need to be grounded to align the fermi level and to make sure that the sum of work function and the kinetic energies in the analyzer are the same as in the sample. Thus, the measured binding energies in analyzer are the same as in the sample, as shown in Fig. 2.11 .

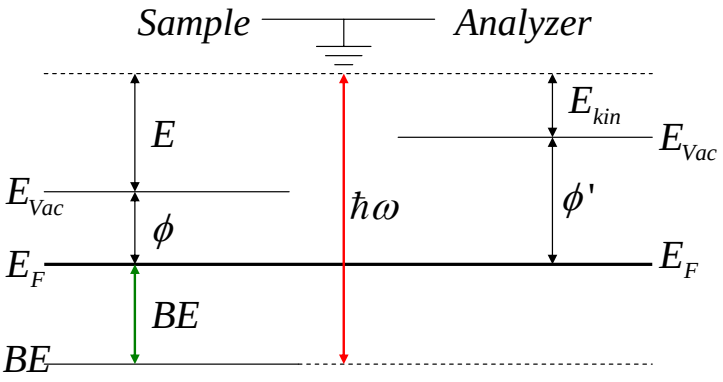

Figure 2.11: The sample and analyzer are grounded to ensure the kinetic energy E_{kin} measured in analyzer is the same as measured in sample.

2.7 Ultrahigh Vacuum System

2.7.1 Why is UHV needed

Gas molecules in a vacuum chamber impinge on samples, and can sticks to them. All kinds of adsorbed molecules form an adlayer on the topmost atomic layers of the sample. The chemical composition and geometrical structure of this contamination adlayer are not well defined. When the vacuum is sufficiently high, one can at least neglect the influence of the gas phase or of adsorbed contaminants, so the sample can be clean for measurement and study for a longer time.

We can derive the pressure we need by estimation of impinging rate. The ambient pressure p determines how many particles of the residual gas impinge on a surface area of $1cm^2$ per second(impinging rate : z$[cm^{-2}s^{-1}]$) through the relationship

$$p = 2m < v > z \tag{2.16}$$

m is the mass of the gas atom or molecules, and $< v >$ is their average thermal velocity with $m < v >^2 /2 \backsimeq 3kT/2$,where T is the temperature in Kevin,and k_B is Boltzmann's constant. Thus we can express p as $p = z\sqrt{2\pi m k_B T}$. And

assume the capacity to accommodate one monolayer of 3×10^{14} particles with an average molecular weight 28 and a temperature of 300K. We can obtain the pressure p approximately equal to 5×10^{-6} Torr. It means the number of molecules build up a monolayer of adsorbate that strikes the surface every second at the pressure of 10^{-6} Torr. In order to keep a surface clean over a period of several hours, it's necessary to have a vacuum with a residual gas pressure lower than 10^{-10} Torr where contamination effects can be neglected.

2.7.2 How to get UHV

Ultra High Vacuum (UHV)provides an environment with a pressure ranging 10^{-9} 10^{-10} Torr. Typically, modern UHV equipment consists of a stainless-steel vessel, the UHV chamber, the pumping station including different pumps, and pressure gauges covering different pressure ranges. Sometimes, a mass spectrometer is also attached to the main chamber to monitor the residual gas.

A combination of different pumps is necessary since there is limited working pressure range for each pump, as shown in Fig. 2.12. In order to lower the pressure from atmosphere(760 torr) to 10^{-10} Torr, we use rotary pump as a backing pump first. Then a turbomolecular pump can be started at about 2×10^{-2} Torr and can lower pressure down into $10^{-6} \sim 10^{-7}$ Torr. Then a ion pump is turn on to pump down the the pressure to 10^{-8} Torr. To achieve UHV ,the procedure of baking chamber is necessary to desorbed the sticky molecules, specially waters, from the inner wall of the chamber. The baking process has to take at least two days at the temperature of $150° \sim 180°$. After bakeout, we need to degas all the filaments of

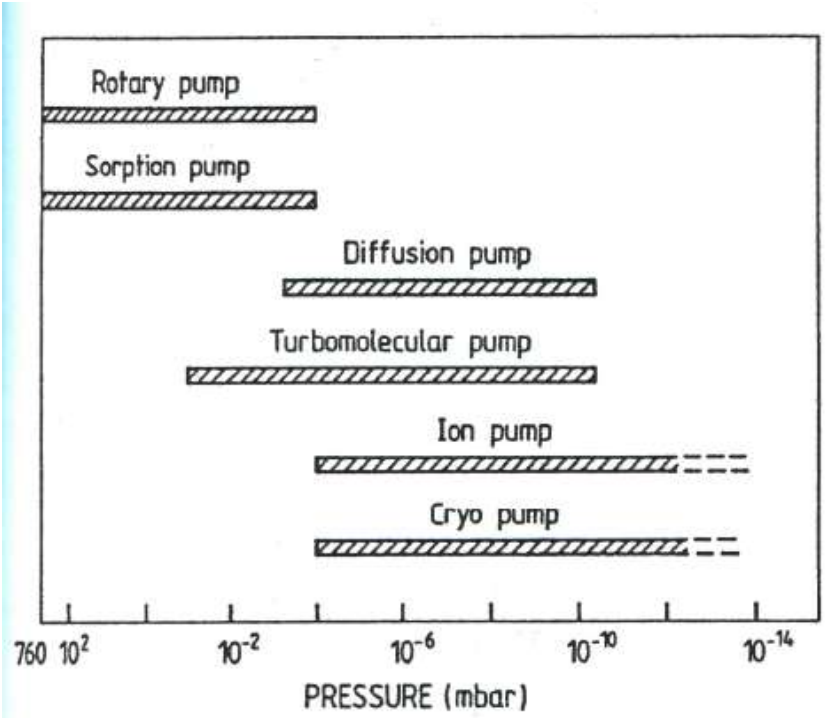

Figure 2.12: Pressure ranges in which different types of pumps can be employed

the instruments equipped on the chamber to remove impurities from the filaments. Then, the chamber will be cooled for half a day and the pressure should be down to 3×10^{-10} torr or less if the chamber doesn't have a leak.

Chapter 3

Surface Systems and Thin Films

3.1 Crystal Lattices and Surface Lattices

An ideal crystal is constructed by infinite repetition of identical groups of atoms, so the crystal lattice can be expressed by small basic units, denoted by crystal lattice vectors. Crystal lattice can be mapped by the repetition of the unit cell defined by minimum volume through translational symmetry. There are several types of unit cells in crystal lattices. The most basic class of conventional cells consist of various types of cubic lattices, eg. Simple Cubic(*SC*), Face-Centered Cubic(*fcc*), Body Centered Cubic(*bcc*)...etc. Lead (Pb), as depicted in Fig. 3.1 (a), forms *fcc* structure with lattice constant $a = 4.95\mathring{A}$. Germanium(Ge) is a diamond structure crystal with lattice constant $a = 5.658\mathring{A}$, as shown in Fig. 3.1 (b). The diamond structure is regarded as a *fcc* lattice with a two-point basis with one atom at the origin and the other located at the position $\overrightarrow{R} = 1/4\hat{x} + 1/4\hat{y} + 1/4\hat{z}$.

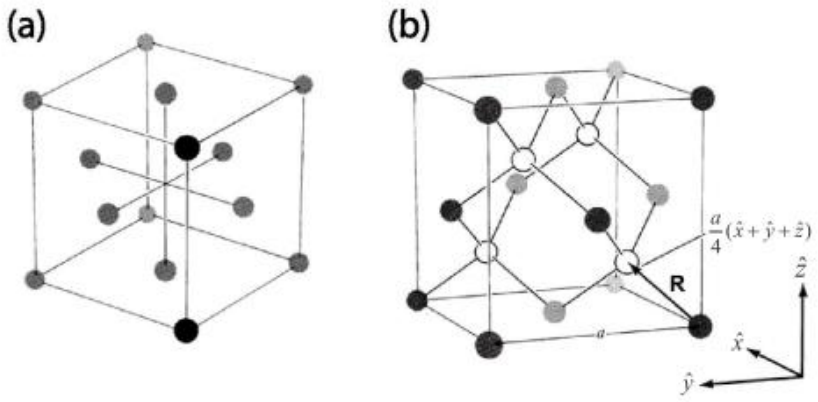

Figure 3.1: (a)The structure of an *fcc* lattice. (b)The structure of a diamond lattice, with displacement in both real and momentum space.[16]

3.1.1 Reciprocal Space

The electronic structure and scattering properties in a crystal are defined by reciprocal space of crystal lattice, which is also called k-space. The reciprocal lattice consists of the set of all the reciprocal vectors that yield plane waves with the periodicity of a crystal Bravais lattice. The reciprocal space is itself a Bravais Lattice and the transformation between direct and momentum space is reflexive for cube lattices. The primitive translation vectors of the *fcc* lattice are

$$\mathbf{a}_1 = \frac{1}{2}a(\hat{\mathbf{y}} + \hat{\mathbf{z}}) \;\; ; \mathbf{a}_2 = \frac{1}{2}a(\hat{\mathbf{z}} + \hat{\mathbf{x}}) \;\; ; \mathbf{a}_3 = \frac{1}{2}a(\hat{\mathbf{x}} + \hat{\mathbf{y}}). \tag{3.1}$$

where a is the side of the conventional cube. The primitive translation vectors of the lattice reciprocal to the *fcc* lattice are

$$\mathbf{b}_1 = \frac{2\pi}{a}(\text{-}\hat{\mathbf{x}} + \hat{\mathbf{y}} + \hat{\mathbf{z}}) \;\; ; \mathbf{b}_2 = \frac{2\pi}{a}(\hat{\mathbf{x}} - \hat{\mathbf{y}} + \hat{\mathbf{z}}) \;\; ; \mathbf{b}_3 = \frac{2\pi}{a}(\hat{\mathbf{x}} + \hat{\mathbf{y}} - \hat{\mathbf{z}}) \tag{3.2}$$

These are primitive translation vectors of a *bcc* lattice, so the *bcc* lattice is recip-

rocal to the *fcc* lattice. The bulk Brillouin Zone of *fcc* lattice can be drawn as shown in Fig. 3.2. The coordinates of high symmetry points are labeled in Table 3.1.

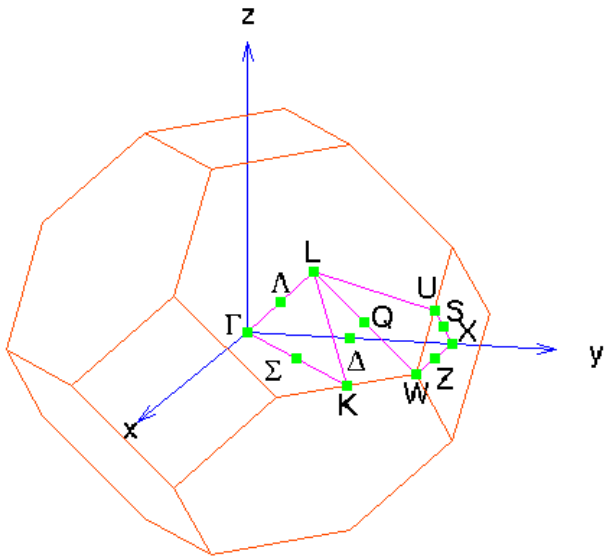

Figure 3.2: Brillouin Zone of *fcc* structure [12].

point	coordinate($\frac{4\pi}{a}$)
Γ	(0, 0, 0)
L	($\frac{1}{4}$, $\frac{1}{4}$, $\frac{1}{4}$)
W	($\frac{1}{4}$, $\frac{1}{2}$, 0)
X	(0, $\frac{1}{2}$, 0)
K	($\frac{3}{8}$, $\frac{3}{8}$, 0)

Table 3.1: Coordinates of points of higher symmetry in the first Brillouin Zone of the *fcc* lattice [4].

3.1.2 Crystal Surface

In a real system, a crystal does not extend infinitely but rather possess a surface. The surface of crystal depends on particular plane which terminates the bulk lattices. And the spacing between crystal planes depend on the plane orientation and particular crystal basis. The termination of crystal alters its reciprocal space and the electronic structure. However , different planes determine different Surface Brillouin Zones(SBZ). For example, Pb(111) plane exhibits six-fold symmetry , as the set of $< \bar{2}11 >$ directions repeats at 60° intervals with the $< \bar{1}10 >$ directions offset by 30° , as shown in Fig 3.3(a) . The high symmetry points of Pb(111) surface are $\bar{M}$ and $\bar{K}$, where $\overline{\Gamma M} = \sqrt{2}\pi/(a\cos 30°)$ and $\overline{\Gamma K} = \sqrt{2}\pi/(a\cos^2 30°)$. And Ge(001) plane exhibits four-fold symmetry , the high symmetry points expressed by $\bar{M}$ and $\bar{X}$, where $\overline{\Gamma M} = 2\pi/a$ and $\overline{\Gamma X} = \sqrt{2}\pi/a$, as shown in Fig 3.3(b).

3.2 Surface Reconstruction

The bulk termination of a crystal surface often results in rearrangement of atoms and bonds driven by energy minimization. The surface atoms can configure into a stabilized reconstruction that is characterized by a $2D$ periodicity. The surface construction is usually expressed in coordinate related to the bulk periodicity with 1×1 unit cell. Wood's notation is the simplest and frequently used method to describe a surface structure, as $(n \times m)R\theta$. The denotation means a periodicity of n bulk units by m bulk units with θ degree rotation. Fig 3.4 displays some typical reconstructions for the (111) and (001) surfaces.

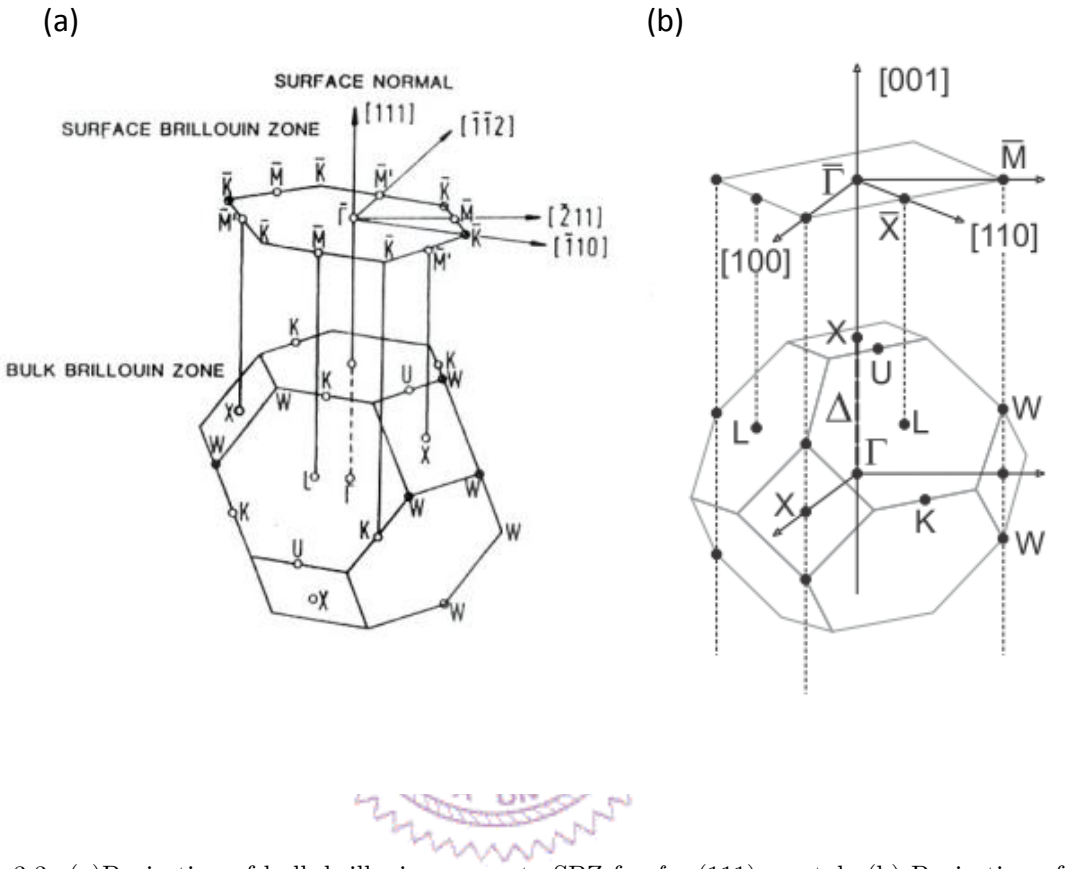

Figure 3.3: (a)Projection of bulk brillouin zone onto SBZ for *fcc* (111) crystal. (b) Projection of bulk brillouin zone onto SBZ for *fcc* (001) crystal.[14].

3.2.1 Reconstruction of Ge(001)

The (001) surface of germanium is prototypical example of system possessing both a strong short-range reconstruction and a moderate-range, energetically weaker one. The 1×1 structure is shown schematically in Fig. 3.5(a), and the simple bulk termination leaves two dangling bonds per surface atom. The short-range interaction is generally accepted to entail formation of dimers by nearest-neighbor surface atoms producing a nominal (2×1) surface phase, as shown in Fig. 3.5(b). The bond formation utilizes one dangling bond per surface atom. The LEED pattern

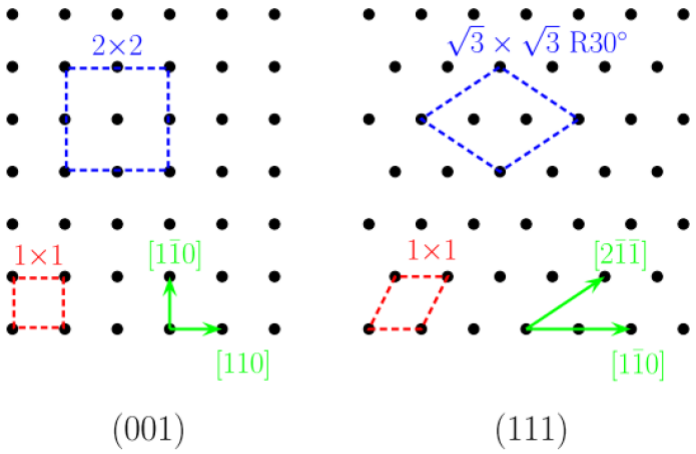

Figure 3.4: Examples of reconstructions for (111) and (001) surface [13].

indicates two-domain 2×1 surfaces, as shown in Fig. 3.6.

A similar mechanism could further lead to the c(4×2) ordering: when the temperature is cooled to 185K from room temperature, the second dangling bond per surface atom interact weakly with those on nearest-neighbor surface dimers. Fig. 3.7 shows the temperature dependence of the LEED patterns, indicating the transition from 2×1 to C(4×2) structure for clean Ge(001) surface.

3.3 Low Energy Electron Diffraction(LEED)

Low Energy Electron diffraction(LEED)is used as the technique to check the crystallographic quality of a surface, prepared either as a clean surface or ordered adsorbate overlayers. In this experiment, a beam of electrons of a well-defined low energy between $20 \sim 500$ eV incident normally on the sample and the elastically

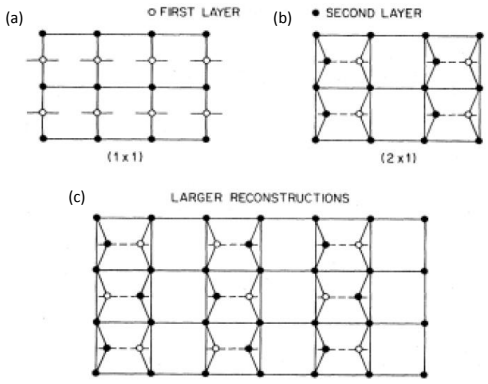

Figure 3.5: Schematic representation of the Ge(001) surface. (a)Simple bulk termination yielding two dangling bonds per surface atom. (b) asymmetric dimerization of nearest-neighbor surface atoms forming a (2×1) unit cell. Open circles indicate surface layer atoms buckled inwards, while solid circles indicate atoms buckled outwards. (c)c(4×2) unit cell formed by alternating the orientation of nearest-neighbor dimers [17].

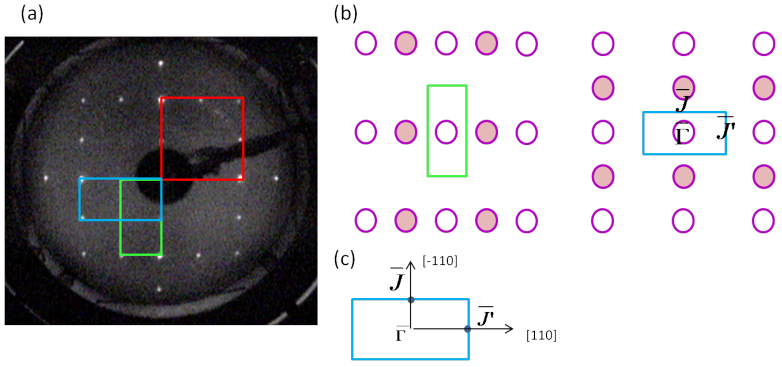

Figure 3.6: (a)The observed LEED pattern of two-domain Ge(001) 2×1 surface at 50eV. 1×1 unit cell is indicated as red solid region. (b) Schematic lattice structure in reciprocal space and the open circles indicate the original lattice points of 1×1 unit cell(c)The 2×1 surface brillouin zones .

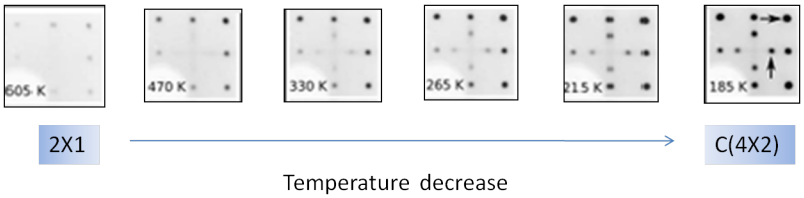

Figure 3.7: LEED imges obtained at temperatures from 185 to 760K. The LEED pattern of 2×1 turns into C(4×2) slowly with temperature decrease. The transition temperature is about 220K. [7].

backscattered electrons give rise to diffraction(or Bragg) spots that are imaged on a phosphorous screen. The observed LEED pattern is a representation of the reciprocal net of the pseudo-2D surface structure. We can use LEED pattern to determine surface structure by Fourier Transform. If the surface is well-ordered, the LEED pattern will exhibit sharp spots with high contrast on low background intensity. But if there are defects or crystallographic imperfections, they will broaden the spots and increase the background. According to de Broglie relation, the wavelength of the electron can be expressed by

$$\lambda = \frac{h}{p} = \frac{h}{\sqrt{2meV}} \tag{3.3}$$

where h is Plank's constant, p is electron moment. For electron kinetic energy $20eV$, the wavelength is about 2.7 Å. It's comparable with atomic spacings,which is the condition for diffraction effects due to the mean free path in the solid. Furthermore, the low electron energy is suited for the studies of surfaces and thin films.

The set up of LEED optics is exhibited in Fig. 3.8. Electrons are emitted from heated filament and accelerated by a Wehnelt cylinder W followed by an electrostatic lens with apertures A, B, C, D. The acceleration energy ($20 \sim 500eV$) is

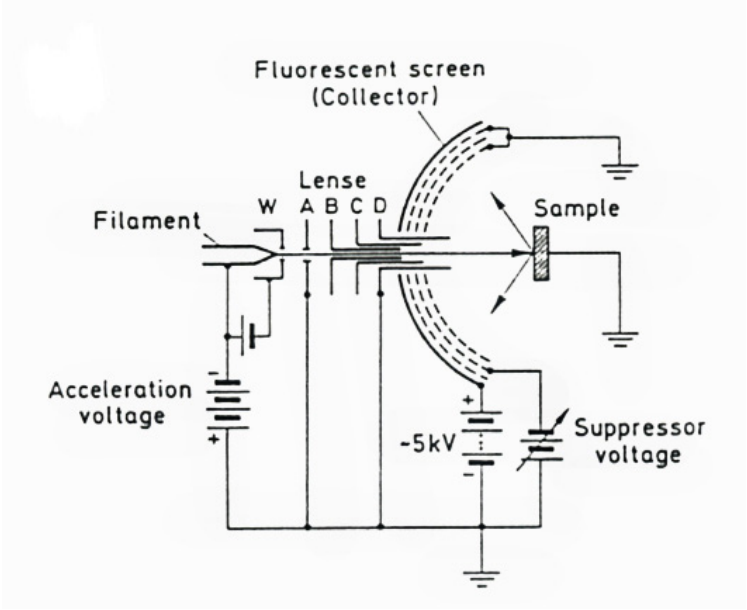

Figure 3.8: Schematic of a LEED optics for electron diffraction experiments [2].

determined by the potential between the cathode and apertures A and D. The lower energy (secondary) electrons are removed by energy-filtering grids placed in front of the fluorescent screen that is employed to display the pattern.

Consider one dimensional case as shown in Fig. 3.9. The condition of an elastic Bragg diffraction is given by constructive interference,

$$d \sin \varphi = n\lambda \tag{3.4}$$

where d is the interlayer distance, φ is the angle between incident and scattered electrons. n is an integer number denoting the order of diffraction. This is a simple model for the scattering of electrons by atoms in topmost layer of solid.

If we consider $2D$ case, the diffraction condition must be fulfilled in both directions. And we can use another formulas to express the diffraction condition which are called Laue Conditions.

$$\overrightarrow{a_1} \cdot \Delta \overrightarrow{k} = 2\pi\nu_1 \quad ; \quad \overrightarrow{a_2} \cdot \Delta \overrightarrow{k} = 2\pi\nu_2$$

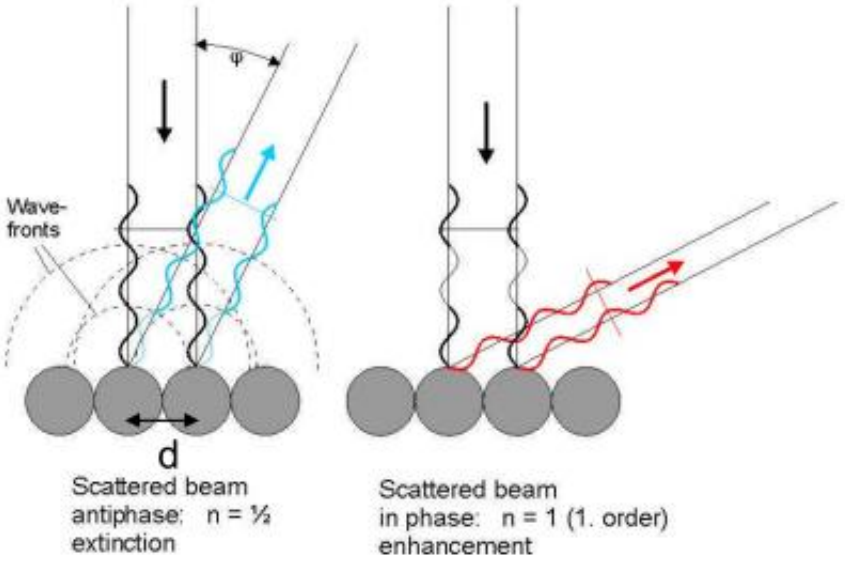

Figure 3.9: Schematics of diffraction condition for one-dimension chain model .[3].

$\Delta\overrightarrow{k} = \overrightarrow{k'} - \overrightarrow{k}$; ν_1, ν_2 are integers.

Here $\overrightarrow{k'}$ and $\overrightarrow{k}$ are the wavevectors of incident and scattered electrons ; $\Delta\overrightarrow{k}$ is the change in wavevector ($\overrightarrow{k'}$ and $\overrightarrow{k}$) and it's called scattering vector. $\overrightarrow{a_1}$ and $\overrightarrow{a_2}$ are primitive vectors of crystal lattice.

It means that the scattering vector component parallel to the surface must equal to the reciprocal lattice vector $\overrightarrow{G_\parallel}$,

$$\Delta\overrightarrow{k} = \overrightarrow{k'_\parallel} - \overrightarrow{k_\parallel} = \overrightarrow{G_\parallel}$$

where $\overrightarrow{k_\parallel}$ and $\overrightarrow{k'_\parallel}$ are the components parallel to the surface of $\overrightarrow{k'}$ and $\overrightarrow{k}$ .This condition is valid for the limiting case where only the topmost atomic layer is involved in scattering. Generally, the incident electron beam hit the sample in the normal

direction, which $\overrightarrow{k_{\parallel}} = 0$. Thus, equation can be simplified to

$$\Delta \overrightarrow{k} = \overrightarrow{k'_{\parallel}} = \overrightarrow{G_{\parallel}} = \frac{\sqrt{2mE_i}}{\hbar} \sin\varphi$$

where E_i is the energy of incident electron beam and φ is the angle between incident and scattered electrons. The possible elastically scattered beams $\overrightarrow{k'}$ can be predicted by Ewald Construction as Fig. 3.10.

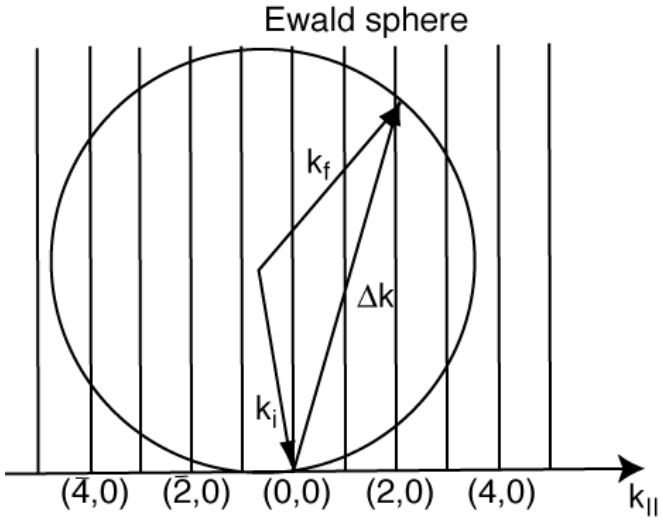

Figure 3.10: The Ewald construction for the surface case . .

3.4 Film Growth

Many factors affect the growth of the films, such as surface energy, interfacial energy, substrate temperature, deposition source, background gas and surfactants. However, there are three different modes to describe the growth of the film phenomenologically as shown in Fig. 3.11. In the layer-by-layer growth mode (or Frank-van der Merve, FM) the interaction between substrate and layer atoms is

stronger than that between neighboring layer atoms. Each new layer starts to grow when the last one has been complete. Conversely, the interaction between neighboring film atoms exceeds the overlayer substrate interaction leads to island growth (or Vollmer-Weber, VW). An intermediate case is the layer-plus-island growth mode. After formation of one, or sometimes several complete monolayers, island formation occurs.

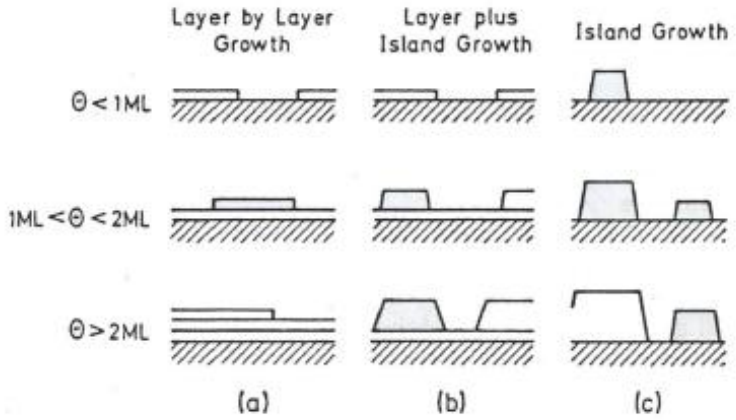

Figure 3.11: Schematic representation of the three important growth modes of a film for different coverage(θ) regimes [2].

3.5 Surface States

Since the real crystals in their nature state are finite, i.e., limited by surfaces, the question arises as to how the energy spectrum of an electron propagating in a finite crystal differs from that in an infinite one. In comparison with the bulk,

surface atoms have fewer neighbors than bulk atoms and part of the chemical bonds which constitute the bulk-crystal structure are broken at the surface. Even an ideal surface with its atoms at bulk-like positions(called truncated bulk) displays new electronic levels and modified manybody effects due to the change in chemical bonding. Generally, surface atoms are displaced from the ideal positions which they would occupy because of the change of chemical bonding near the surface. The general theoretical approach is similar to that for the bulk crystal. In essence the one-electron approximation is used and tries to solve the Schrödinger equation for an electron near the surface. A variety of approximation method may be used to taken into account many-body effects.

Solving the Schrödinger equation for an electron moving in the potential field where the potential is periodic inside the crystal and constant in the vacuum region ,the wave vector is determined by the boundary conditions. For infinite crystal, the wavevector k is real to ensure that the wave function remains finite. Possible surface solutions are standing Bloch waves inside the crystal which are matched to exponentially decaying tails on the vacuum side , as shown in Fig. 3.12(a) . The corresponding electronic levels are therefore only slightly modified from those of the infinite bulk crystal. Additional surface solutions become possible if we allowed complex wave vectors k=p+iq. The wave function is localized near the surface and the energy level lie in the gaps of the projected bulk-band structure, i.e., known as *surface state*. If surface-state bands can penetrate into a part of surface Brillouin zone, where propagating bulk states exist. They are degenerate with bulk states and can mix with them. These states, which will propagate deep into the bulk and will nevertheless retain a large amplitude close to the surface, are known as *surface*

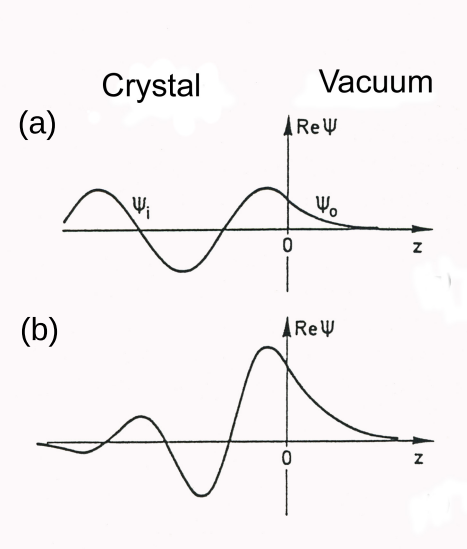

Figure 3.12: Real part of the one-electron wave function (a)a standing wave matched to an exponentially decaying (b) a surface-state wave function localized the surface [2].

resonances.

For the topmost surface atoms, their wave functions have less overlap with wave functions of neighboring atoms. The splitting and shift of the atomic energy levels is thus smaller at surface than in the bulk, as shown in Fig. 3.14. The energetically higher-lying surface state has conduction-band character, whereas the lower level which is split off from the valence band of the semiconductor is more valence-band like. Therefore the charging character of the surface states also reflect that of the corresponding bulk states. A semiconductor is neutral if all the electrons occupied the valence-band states and the conduction-band states are empty. On the other hand, the conduction-band states carry a negative charge if they are occupied by an electron, and the valence-band states are positively charged when being unoccupied. In accordance with the definition of shallow bulk impurities, the surface state derived from the conduction band is called acceptor-type state and the surface state

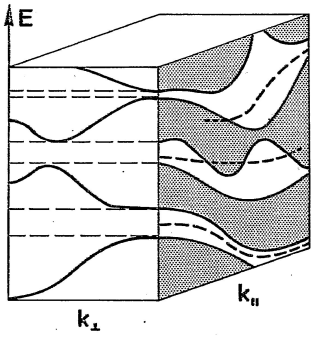

Figure 3.13: The shaded area in the $E(k_{\|})$ plane describe the projected bulk-band structure(along $k_{\perp}$) Broken lines in the $E(k_{\|})$ plane indicate surface states bands in the gaps of the projected bulk-band, and the short dotted lines indicate surface resonances where they are degenerated with bulk states [2].

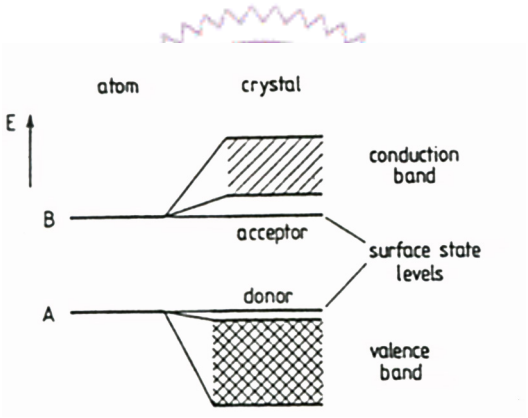

Figure 3.14: Surface states have acceptor-type or donor-type charging character [2].

derived from the valence band is called donor-type state.

So far, the surface states we discuss are all related to the clean and well-ordered surface of a crystal with 2D translational symmetry. These states are called intrinsic surface states. In addition to these states, there are other electronic states localized at the surface which are related imperfections and adsorbed atoms. The imperfections and adsorption cause change in the chemical bonding, thus giving rise

to changes in the spectrum of electronic surface states.

3.6 Quantum Well States

Thin films have been a major playground and tested ground for quantum size effects for electronic devices applications. When films become thin enough, quantum size effects become important. Electrons confined between the potential barriers of the vacuum and the film-substrate interface can be like "particles in a box" so their wavefunctions are like standing waves, forming the so-called quantum well states (QWS). The band gap of the substrate plays a crucial role for QWS. If the film electrons of fall within a gap in the substrate band structure, then the electrons will remain confined in the overlayer. It's often seen in the metal-semiconductor system. However, confinement also can arise in a metal-metal system when the band structure of the substrate exhibits a relative gap in comparison to the film, such as the Ag/Au(111) system [8]. Quantum well states are associated with discrete quantized electronic states in small artificial structures with adjustable physical dimensions. The quantum confinement of the electrons result in the quantization of the electronic wave vector along the direction perpendicular to the film surface. If the states arise from electrons with energies below the substrate valence band, the electrons partially are confined in the film. And these states are called quantum well resonances(QWR). For the Pb/Ge(111) system, the relevant direction in real space is the [111] direction, which is the surface normal for both the substrate and the film and which corresponds to the ΓL direction in k-space. As shown in Fig. 3.15, quantum well states exist in the confinement range between the substrate band

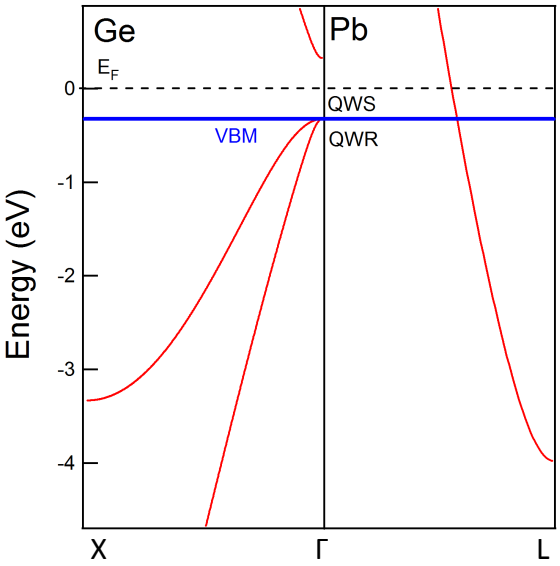

Figure 3.15: Compare the band dispersion of perpendicular to the Pb(111) plane and Ge(001) surface.

maximum and the Fermi level. Most of electronic states that arise from electrons with energies below the substrate valence band but whose wave functions are partially confined are termed quantum well resonances (QWR).

A simple model for electronic motion perpendicular to the film surface is that of a free electron confined in a one-dimensional box. Although this is a very crude model, it serves to illustrate the basic ideas. The allowed wavevector k for quantum well states are determined by the requirement that standing wave patterns fit into the geometry

$$k = \frac{n\pi}{d} \tag{3.5}$$

where n is an integer quantum number and d is the film thickness or bulk dimen-

sion. The energy levels are given by

$$E = \frac{\hbar^2 k^2}{2m} = \frac{\hbar^2}{2m}(\frac{n\pi}{d})^2; \quad \Psi(z) \propto \sin(\frac{n\pi z}{d}) \tag{3.6}$$

where m is free electron mass.

3.6.1 The Bohr Sommerfeld phase model

For a solid film, the $E(k)$ band dispersion is generally different from the free electron dispersion given in Eq.(3.6). Thus, a measurement of E_n can provide useful information about $E(k)$. Note that the quantization condition is given by Eq.(3.5) is valid only for abrupt infinite barrier. For solid-solid and solid-vacuum interfaces, the confinement potential is generally finite and rounded. Thus, the quantization conditions must be modified by a phase shift. This phase shift can be deduced from the energy position of QWS at different thickness of the films. It is an important quantity characterizing the boundary potential. As a confined electron traverses a film, its wave function accumulates the phase shift not only in transition, but also when it is reflected from the substrate interface and the vacuum. The total phase shift must equal to an integer multiple of 2π to fit the condition of constructive interference. It suffices to carry out a simple analysis based on the Bohr-Sommerfeld quantization rule

$$2k_\perp(E)Nt + \phi_i(E) + \phi_s(E) = 2n\pi \tag{3.7}$$

where $k_\perp$ is the electron wave vector perpendicular to the interface, E is the energy of the state, N is the number of the monolayer, t is the monolayer thickness, ϕ_i and ϕ_s are the energy dependent phase shift at the surface and interface, respectively; and n is a quantum number. This is the same as requiring the de Broglie wave

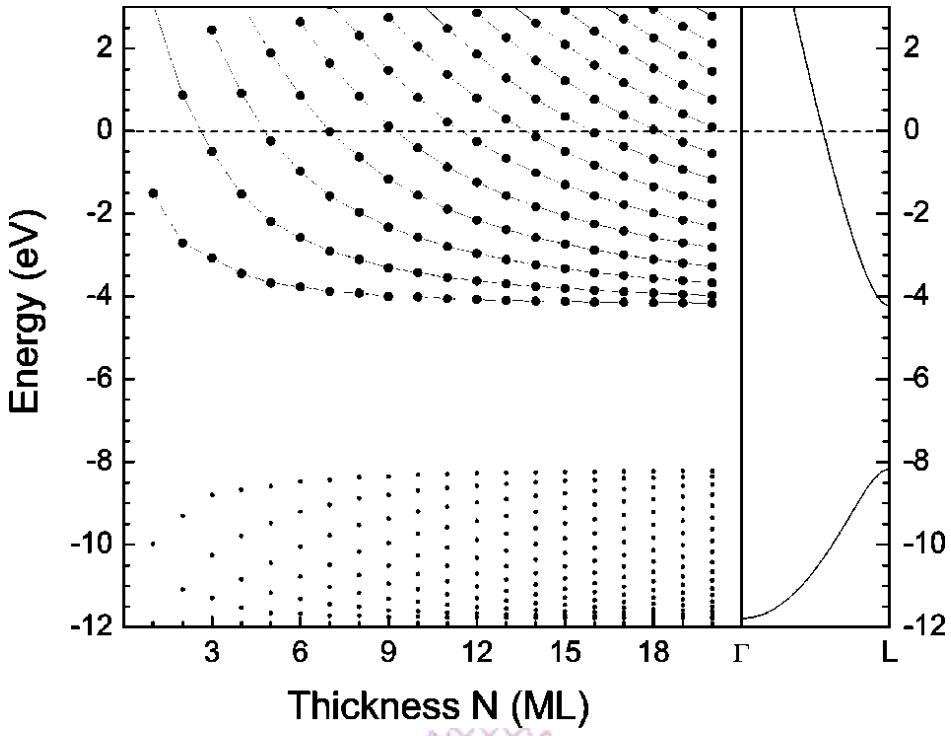

Figure 3.16: Calculated quantum well state energies for a standing Pb film. The dashed line indicate the same quantum number [31].

associated with the the electron to form a standing wave. Eq.(3.7) can be traced back to the beginning of classical mechanics for standing waves. Eq.(3.5) is a special case of Eq. (3.7) with Φ=0(or 2π).

Thus, the quantum well state energy levels can be determined by the Bohr-Sommerfeld quantization rule for each set of integers N and n. Fig. 3.16 shows the theoretical spectrum of quantum well state energies at the surface brillouin zone center (normal emission) for free-standing Pb film over a range of thicknesses. A change in thickness of only one atomic layer noticeably alter the electronic structure. At lower thickness, the electron energies are spaced relatively far apart, but their separation decreases as the thickness increases. However, the energy states appear continuous as the film become bulk-like.

3.6.2 Quantum number

In Eq.(3.5), one can choose to measure $k_\perp$ from the zone center (Γ point) or the zone boundary at the L point. The quantum number depends on the origin where we chose. Conventionally, the zone boundary is chosen as the origin. And the wave vector is limited in the direction perpendicular to the surface without the parallel components. The Eq.(3.7) can be rewritten as

$$k_\perp = \frac{n\pi}{Nt} - \frac{\phi}{2Nt} \tag{3.8}$$

where $\phi = \phi_s + \phi_i$ is the total phase shift.

A film is invariant under a translation of t in the direction perpendicular to the surface, where t is the monolayer thickness. Thus, it can be considered as 1D periodic lattice with primitive vector of real space $\mathbf{a} = a\hat{x}$ in the perpendicular direction of the surface, as shown in Fig. 3.17. In the reciprocal lattice, the reciprocal vector $\mathbf{b}$ is equal to $2\pi/a$, so the distance between the zone center and the zone boundary is equal to $\frac{\pi}{a}$. The distance from the zone center to the zone boundary at L is $\frac{1}{2}\Delta k_{\Gamma L\Gamma} = \pi/t$. If the phase shift is zero, the wave vector $k_\perp$ satisfing Eq.(3.8) divides the region between the Γ and L point into N parts. For this simple case, the allowed $k_\perp$ is integer n times π/Nt . Thus, the quantum number is labeled from 0 to N for N monolayer thin film. And the wave vector of the state corresponding to $n = 0$ is at the zone center and the $n = N$ is at the zone boundary. When the phase shifts at the surface and interface are taken into account, the allowed wave vectors corresponding to the quantum well states will shift.

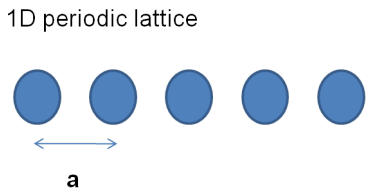

Figure 3.17: One dimensional periodic lattice with lattice constant a. .

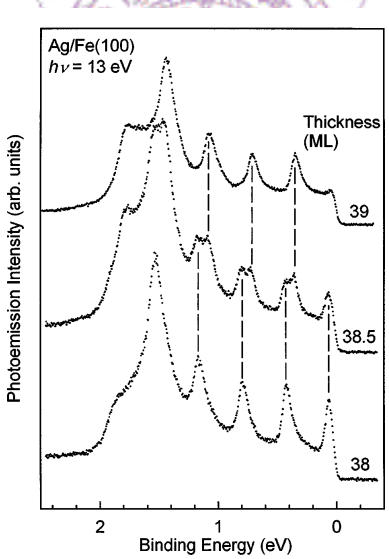

Figure 3.18: Normal Emission spectra from the valence region of 38ML, 38.5ML and 39ML Ag films on Fe(001) taken at a photon energy of 13eV. The quantum well state peak positions are indicated by the vertical line. [15].

3.6.3 Atomic Layer Resolution

Fig. 3.18 illustrate the experimental resolution of individual layer thicknesses. Photoemission spectra taken at a photon energy of 13 eV are shown for layer thicknesses of 38, 38.5 and 39 ML. These layers were prepared by first growing a nominally 38 ML thick film in one step and adding very small amounts of Ag at lowtemperatures with subsequent annealing steps until a uniform layer showing just one set of quantum well peaks was obtained. The corresponding spectrum is shown as the bottom trace in Fig. 3.18. Subsequently 0.5 ML of Ag was added to yield the 38.5 ML spectrum, which exhibits two sets of quantum well peaks. One set is at the same position as the 38 ML case, and the newly emerged set is at somewhat lower binding energies and must correspond to a thickness of 39 ML. This is verified by adding another 0.5 ML to yield the 39 ML spectrum. The set of peaks corresponding to 38 ML is now completely suppressed, and only the 39 ML peaks remain. The same discrete layer behavior has been seen for many different starting thicknesses [15].

If the overlayer or substrate is not optimally prepared, several layer thicknesses can be simultaneously present, giving rise to a large number of peaks. Films with even lower qualities exhibit broad line shapes, where peaks from individual thicknesses can no longer be detected.

Chapter 4

Pb Films on Ge(001)

4.1 Introduction

Metal-semiconductor systems continue to be of great interest in basic research and technology. Especially for the adsorption of Pb on Si and Ge surfaces, it has attracted considerable interest over the past few years [18, 13]. Pb atoms show very low solubility in the Si(Ge) bulk environment, so Pb on Si and Pb on Ge are considered as prototype examples for abrupt metal-semiconductor interfaces. Most invetigations were focused on Pb/Si(111) [13] and Pb/Ge(111) [19] systems, where a variety of different 2D phases have been found, depending on the exact coverage, heat treatment and temperature [21]. Recently some research groups started to study the Pb/Ge(001) system [22].

D.Cvetko *et al.* have found that by Helium Atom Scattering(HAS) that Pb films grow layer-by-layer at low temperature in (111)orientation, rotated by 45° with respect to the Ge(001) substrate. The monatomic step height between terraces was found to depend on the thicknesses of Pb layers and to display an oscillating behavior. Simultaneously no lateral variations of the surface unit cell size has been

detected. The oscillation of step height thus can be attributed to quantum size effect(QSE) [26, 25].

Yang *et al.* reported the surface superstructures of Pb/Ge(001) system as well as the phase transitions observed by LEED pattern and Scanning Tunneling Microscopy (STM) with thickness variation [27].

In our work, there are mainly two topics to discuss. The first topic is the interaction between the Ge(001) substrate and Pb films, investigated through energy band dispersion of QWS subbands, as measured by ARPES. The other one is the layer resolution of Pb films, as exhibited in photoemission spectrum.

4.2 Experiment

In our study, angle-resolved photoemission measurement was performed at the National Synchrotron Radiation Research Center (NSRRC). A clean Ge(001)-2×1 surface was prepared via several cycles of 1 keV Ne^+ bombardment at 450° for 15 minutes followed by 15 minutes of annealing at 550°. The heating method is electron beam bombardment ; a heated filament at a distance of about 1cm from the rear side of the sample produce the thermionic emission, and the filament is biased at about 100∼200 V relative to the sample to accelerated the electrons toward the sample. The cleanness of the sample was confirmed by observing the sharp 2×1 LEED pattern at room temperature.

Then Pb atoms were deposited on clean Ge(001) surface no more than one monolayer at room temperature, followed by annealing to 250° in order to form the c(4×8)

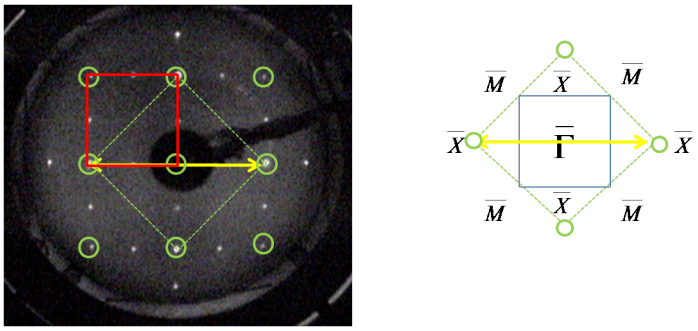

Figure 4.1: The LEED pattern of clean Ge(001) surface and its corresponding surface brillouin zone (blue solid region). The red solid region indicates 1×1 unit cell in the reciprocal space. .

wetting layer. Subsequently, more Pb was evaporated onto the wetting layer at T=-150° from the K-cell evaporator. According to the interval between adjacent QWS peaks of maximum intensity, we could identify the evaporation time of 1ML, to calibrate the deposition rate. According to this rate, we could derive the absolute coverage scale.

Photoemission data was taken a series EDC and displayed as two-dimensional image with the energy and the polar emission angle. The emitted angle of image was ±10°. The sample was rotated relative to analyzer in step of 6° to create a set of overlapping images, which were combined with various emitted angles. The band dispersion was measured along the $\overline{\Gamma X}$ direction of Ge(001) surface brillouin zone, as indicated in Fig. 4.1. To distinguish the bulk state band from the surface state band, different photon energies were employed for measurement.In contrast to the bulk state, the peak position of a surface state is independent of the photon energies used.

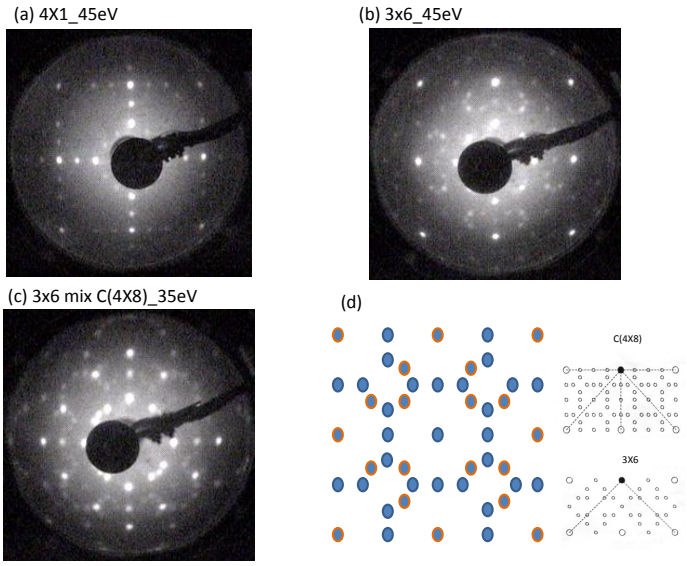

Figure 4.2: Different Pb superstructures in different deposition rates were exhibited in LEED pattern. (d) Schematics representation of mixing between 3×6 and c(4×8) phase. .

4.2.1 Wetting Layer Surface State

As mentioned in previous section, we made a wetting layer first before depositing overlayer Pb films. Three different phases of wetting layers such as 3×6, 4×1 and $c(4 \times 8)$ were observed, depending on the amounts of Pb atoms on Ge(001). Fig. 4.2 shows the LEED patterns of these three surface reconstructions. We found that overlayer Pb films can grow layer-by-layer on each of the three different wetting layers, as demonstrated by Fig. 4.3, in which the EDC of QWS from Pb films grown on one wetting layer can match another one grown on different wetting layers.

As seen, Fig. 4.4 shows the photon energy dependence of EDC's at normal emission for $c(4 \times 8)$ phase of the wetting layer, there are two apparent peaks at 1.38 eV and 0.27 eV below the fermi level for c(4×8) phase at normal emission. We find that the peaks observed at -1.38 eV and -0.27 eV are surface states, because their peak positions are not changed for different photon energies.

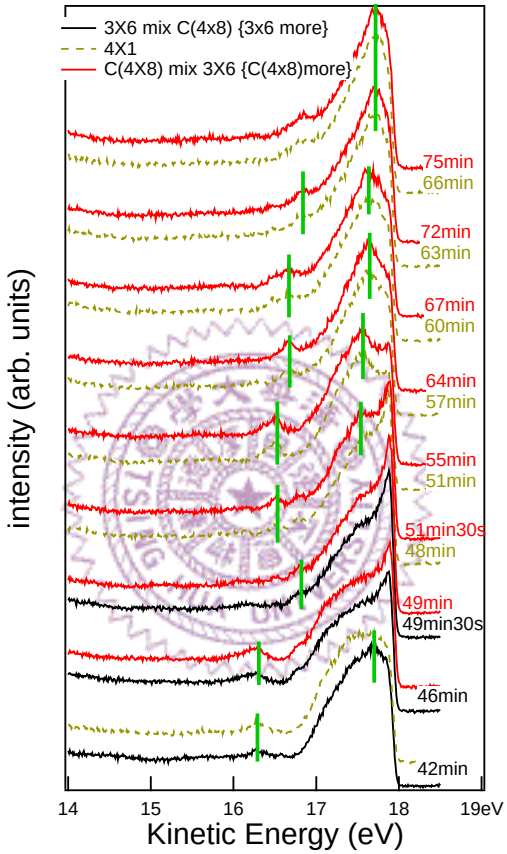

Figure 4.3: Comparison of the normal emission curve in different wetting layer structure. Each curve can be matched with other curve in different deposition rate. .

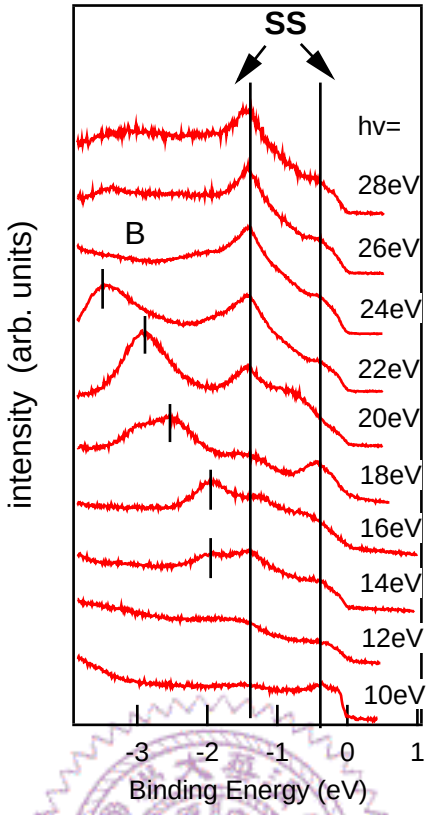

Figure 4.4: The surface state peaks of c(4×8) phase will not shift as the photon energy changes. SS indicates the Surface state and B indicates the Bulk state. .

4.2.2 Theoretical Method

In addition to the measured energy band dispersions of QWS in Pb films on Ge(001), we also calculated the Pb subbands for each integer layers for comparison by *Static* tight-binding program [12]. Before band calculation, we have to determine the quantum well energy positions at normal emission by the Bohr-Sommerfeld quantization condition as described in Eq.(3.7):

$$2k_{\perp}(E)Nt + \phi_i(E) + \phi_s(E) = 2n\pi$$

where $k_{\perp}$ is the electron wave vector along the $L\Gamma$ direction in Pb(111)plane, E is the energy of the state, N is the number of Pb monolayer, ϕ_i and ϕ_s are the energy dependent phase shift at the surface and interface, and $t = 2.86\mathring{A}$ is the

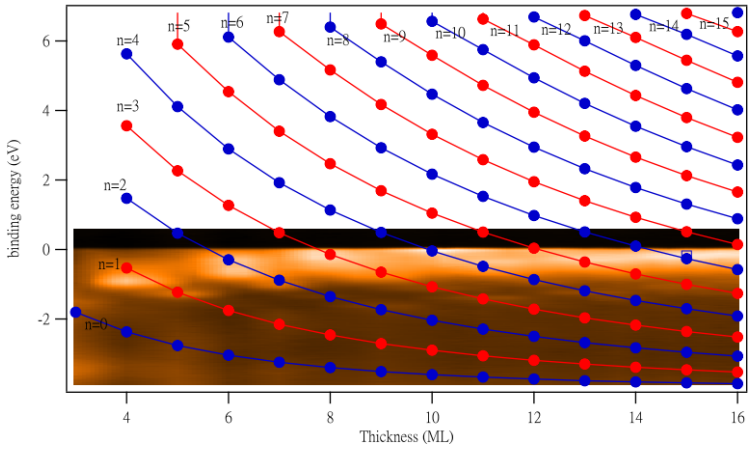

Figure 4.5: Each dotted-curve indicates different quantum number n for different Pb film thickness. Each dot indicates the QWS at each integer layer and each quantum number. .

lattice spacing in (111) direction. This equation determines the allowed wave vector $k_\perp$ values, which in turns, determine the binding energies of quantum well states through the bulk band dispersion relation E($k_\perp$) along the ΓL direction of Pb. In thin film system, $k_\perp$ is quantized in the direction perpendicular to the surface of the film, and $k_\parallel$ remains continuous because the lateral size of the film is usually much larger than the thickness.

We use the binding energies of quantum well states and the Bohr-sommerfeld rule to determine the phase shifts at the surface and interface. The phase shifts can be fitted as a linear function of energies. The binding energies of each quantum well states would be acquired again by fitting process. The measured energies of the QWS at normal emission as well as the fitting results are plotted in Fig. 4.5. Thus, we can use the calculated $k_\perp$'s values for each integer layers as these of the QWS subbands.

4.3 Thickness Dependence of QWS

The image of Fig. 4.6 show the energy distribution curves(EDC) of QWS at normal emission for films ranging in thickness from 0 to 16 ML Pb films on Pb/Ge(001)-c(4×8) surface. According to the tendency of EDC at normal emission with increasing thickness, each QWS peak moves toward the fermi level as the film thickness increasing. There are a set of quantum well state peaks corresponding to each integer monolayer thicknesses. When the intensity of the peak corresponding to N ML decreases, the peak corresponding to N+1 ML begins to emerge. This phenomenon demonstrates that a layer-by-layer growth mode of films. To observe the peak intensity change, we can identify whether the film thickness is at integer layer or not and assign each integer layer to each QWS peaks, as indicated the blue EDCs in Fig. 4.6. Figure 4.7 shows the 2D angle-resolved photoemission spectra of QWS subbands in the direction from $\overline{\Gamma}$ to $\overline{X}$ with respect to the Ge(001) surface brillouin zone for Pb films of thickness 4∼16 monolayers(ML). As seen, the band dispersion are more complex and distorted around the zone center but overall exhibit roughly parabolic dispersions. The distortion of the QWS subbands around the zone center is due to the interaction with Ge(001) substrate band edges.

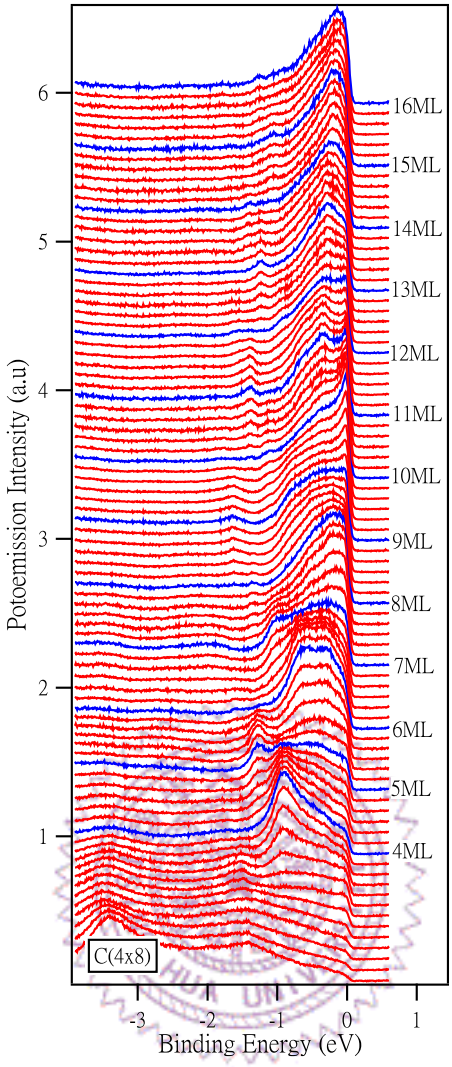

Figure 4.6: Photoemission spectra at normal emission taken from Pb film of thickness N=0∼16ML on the Pb/Ge(001)-c(4 × 8) surface. Blue lines indicate the integer thickness of Pb films. .

In order to understand the interaction with Ge band edges, we try to calculate the Ge bulk bands along the direction parallel to the $\overline{\Gamma X}$. There are infinte bulk subbands along the direction parallel to $\overline{\Gamma X}$. We therefore divide the segment from Γ to X, the direction perpendicular to the (001)surface, into 50 intervals. Each interval has a fixed $k_{\perp}$ value to serve as the origin($k_{||}$=0) of a bulk subband along $\overline{\Gamma X}$ direction.

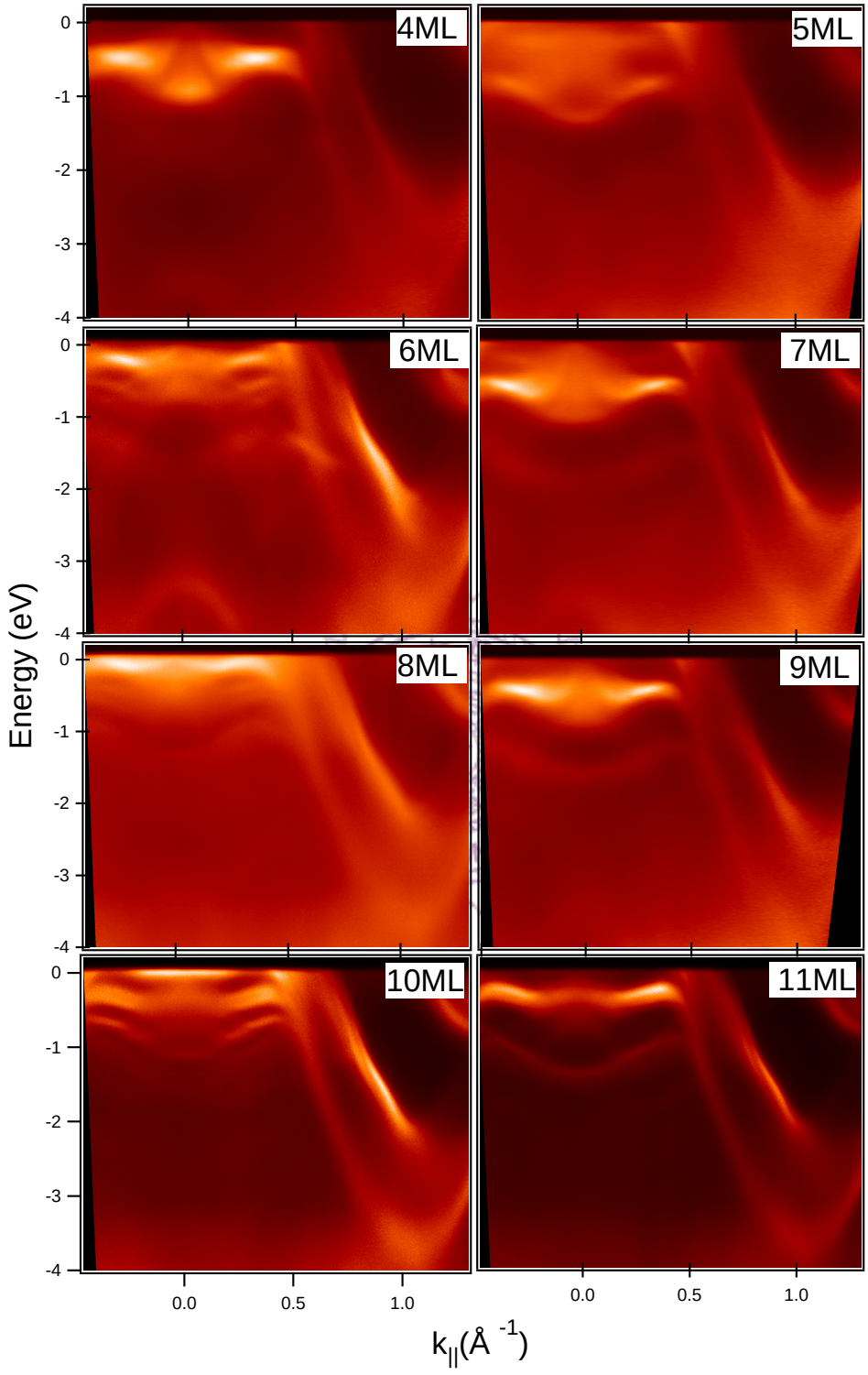

Figure 4.7: The photoemission data presented as gray-scale images for film thickness of each integer layers.

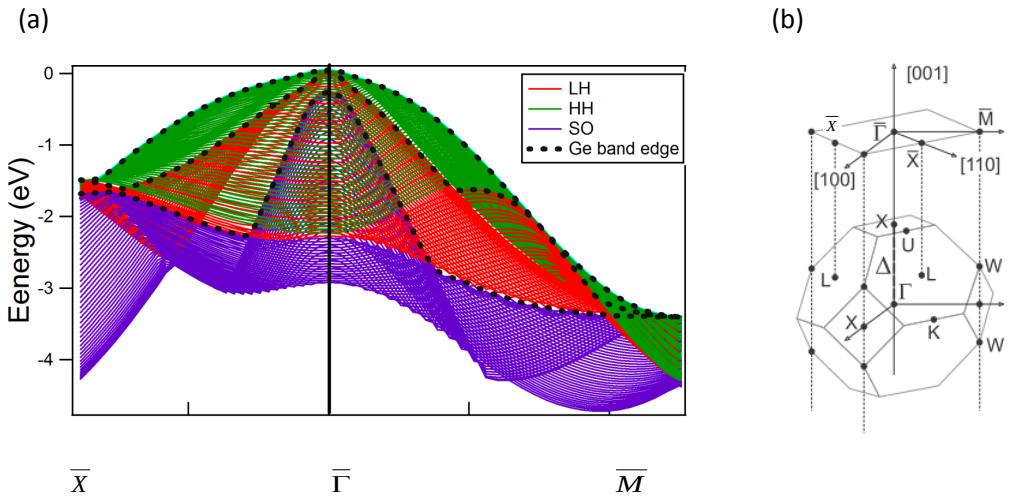

Figure 4.8: (a)The projected bulk bands to the Ge(001) surface. The black dash lines indicate the HH, LH and SO band edges. (b) Schema of calculated direction as the arrows presented.

In this way, we found there were three braches of Ge subbands, which ar the so-called HH, LH and SO bands. The band edge of these three branches were then determined by extract the maximum energies of the subband for the three branches at each $k_{||}$ point.The band edges of these three branches are shown by the dark dot curves in Fig. 4.8. Later we will show how the substrate band edges affect the band dispersion of QWS.

We calculated the QWS subbands of Pb free standing films by tight-binding results of Pb bulk bands. We first determined the allowed discrete $k_{\perp}$ values by Bohr-Sommerfeld quantization rule. Then, we have to decide the dispersing directions of

QWS subbands. The LEED patterns of integer monolayers show 12 spots because of the growth of two (111)domains for the Pb films, as shown in Fig. 4.9(a), and its $\overline{M}(\overline{K})$ symmetry point rotates about 15° with respect to the ($\overline{\Gamma X}$ direction of Ge substrate, so we could define $\overline{\Gamma O}$ as the direction parallel to $\overline{\Gamma X}$ of Ge(001) SBZ and calculate the Pb subbands along this direction at discrete $k_\perp$ values in the ΓL region along Pb(111) plane, as shown in Fig. 4.9(b). In Fig. 4.9(c), we found the projected bulk brillouin zone projected to (111) surface is symmetrical about the $\overline{\Gamma}$ point in $\overline{K\Gamma K}$ direction and is antisymmetrical in $\overline{M'\Gamma M}$ direction. Therefore, the QWS subbands in the direction $\overline{\Gamma O'}$ opposite to $\overline{\Gamma O}$ also has to be taken into account.

We compare the calculated Pb subbands with the QWS subbband dispersions measured by ARPES, as shown in Fig. 4.10. It is interesting that the calculated and measured results matched each other except for the region near the zone center. The deviation is due to the interaction between QWS subbands and Ge band edges.

4.3.1 The interaction between QWS subbands and substrate band edge

Generally, the upper valence band is formed by bonding p-like states in group IV semiconductors such as Ge, while the conduction band is formed by antibonding s-like states. The degeneracy of top of valence band therefore corresponds to three p-orbitals, while the bottom of the conduction band has no degeneracy. For isolated atoms, the coupling between the orbital angular momentum of these states and the electronic spin results in a splitting of the top valence band into heavy holes(HH),

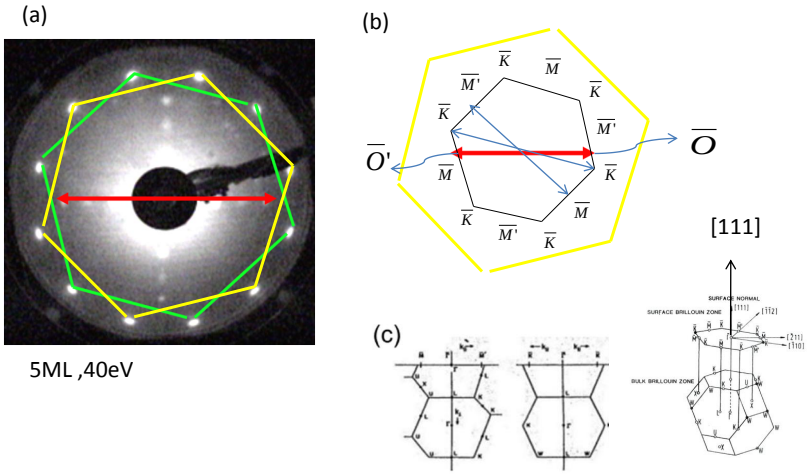

Figure 4.9: (a) The LEED pattern present 12 spots of 5ML Pb film (b) The corresponding surface brillouin zone shows the symmetry points $\overline{M}(\overline{K})$ rotated 15° with respect to the $\overline{\Gamma} - \overline{X}$ direction of Ge. (c) Cuts through the bulk brillouin zone in two directions of the SBZ: the left picture is along $\overline{M'} - \overline{\Gamma} - \overline{M}$ direction and right one is along $\overline{K} - \overline{\Gamma} - \overline{K}$. [14].

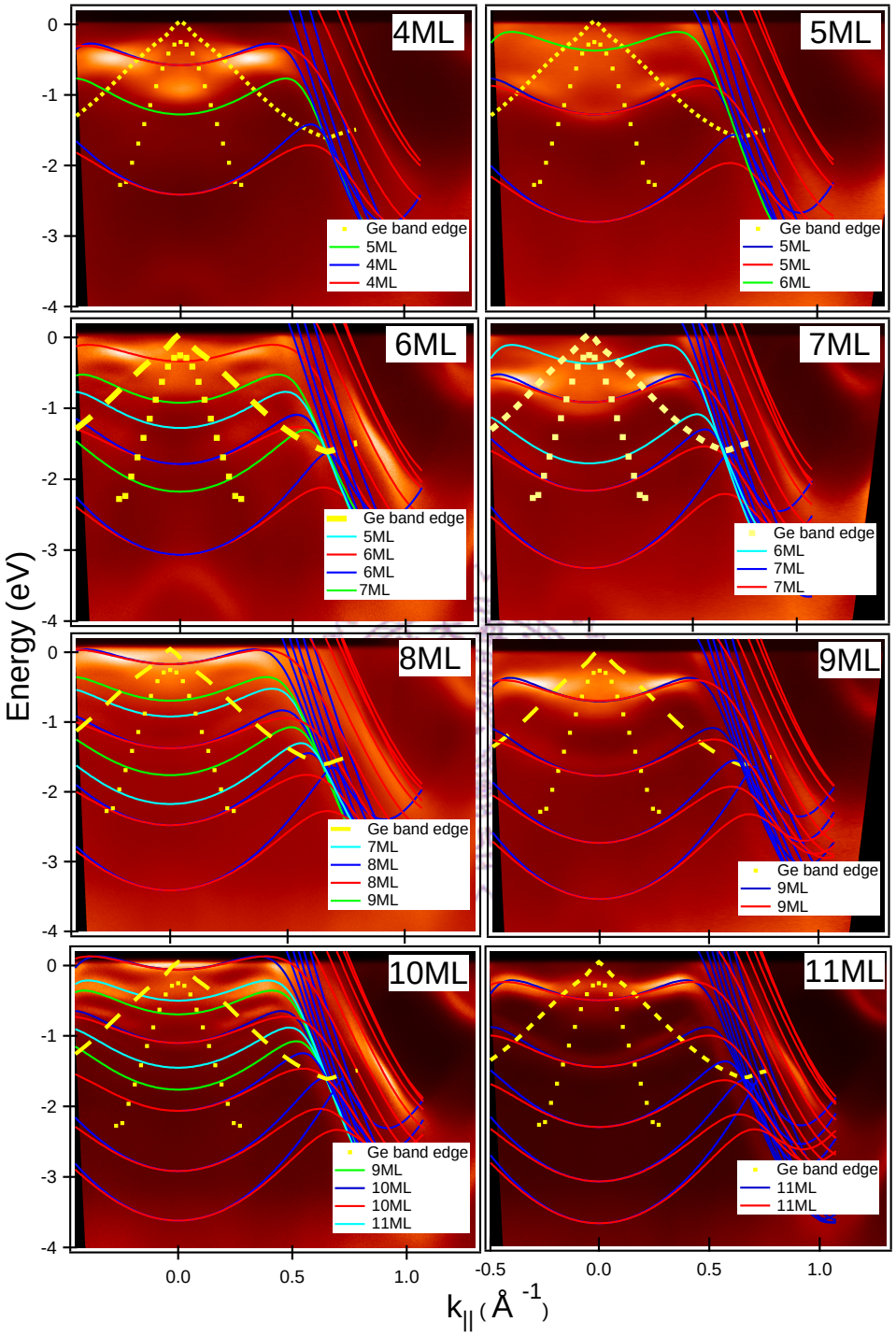

Figure 4.10: The calculated Pb subbands are superimposed onto the photoemission data for film thickness of each integer monolayers.

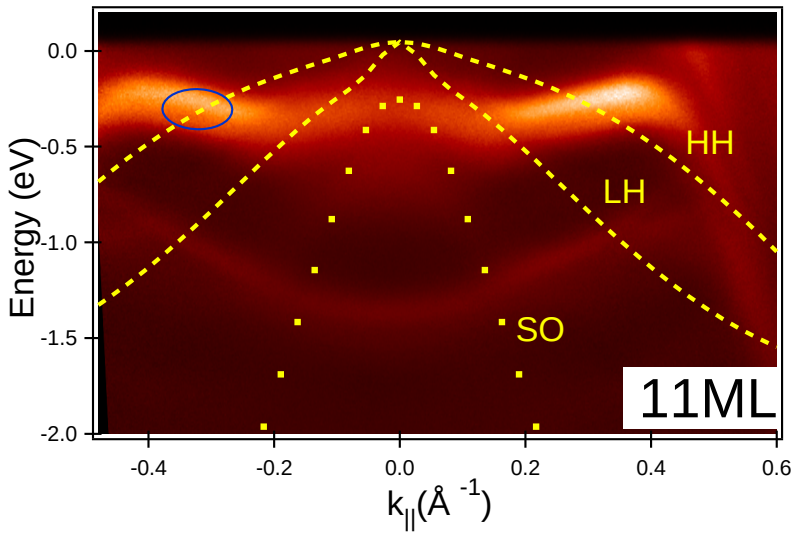

Figure 4.11: Angle-Resolved photoemission data presented as an image as a function of energy and wave vector $k_{\|}$ for 11ML of Pb on Ge(001). The three concave curves present projected bulk band edges in Ge along the $\overline{\Gamma X}$ direction. .

light holes(LH) and split-off holes(SO) [4].

Figure. 4.11 shows 2D photoemission image of QWS subbands for Pb film of 11ML. The three concave curves in Fig. 4.11 represent the topmost projected calculated bulk band edges of Ge. As seen, the topmost band edge, HH, crossed the QWS subbands without causing interaction. In contrast, LH and SO band edges caused the distortion of QWS subbands, which shows a break(kink) at the crossover point. Previous studies on similar systems such as Ag/Si(111)[18] and Ag/Ge(111)[28], however showed HH band edge is the one that has the most interaction with the QWS subbands. Before going to discuss about the discrepancy, we first review the physics mechanism of this interaction.

Consider that a quantum well state Ψ changes, as a function of $k_{\|}$, through the edge of a continuum of substrate states Φ. The situation is similar to that for

the interaction between the impurity (or adsorbate) and bulk, as simuated by the Anderson model [29]. By employing this model,straightforward derivation for the present case yields the retarded Green's function G [28]:

$$G(E)^{-1} = E - E_q + i\delta_q - \int_{-\infty}^{E_0} \frac{|V|^2}{E - \varepsilon + i\delta_s} g(\varepsilon) d\varepsilon$$

where E_q is the energy of the quantum well state without coupling, δ_s and δ_q are the lifetime broadenings of the substrate and the quantum well states, respectively, V is the coupling matrix element between Ψ and Φ, and E_0 is the band edge. The density of state $g(\varepsilon)$ near the band edge has the following one-dimensional form:

$$g(\varepsilon) = \frac{A}{\sqrt{E_0 - \varepsilon}} \Theta(E_0 - \varepsilon)$$

where A is a prefactor proportional to the square root of effective mass and Θ is the unit step function. Assuming the matrix element are constant within the limited range of interest, the integration can be carried out analytically to yield the spectral weight function

$$\rho(E) = -\frac{1}{\pi} Im(G) = -\frac{1}{\pi} Im\left(\frac{1}{E - E_q + i\delta_q - \pi A |V|^2 (E - E_0 + i\delta_s)^{-1/2}}\right) \quad (4.1)$$

The anticrossing behavior is a result of the one-dimensional density of states, which has the divergent, but integrable, singularity at the band edge. The singularity resembles a skewed peak at E_0 with lifetime broadening. The net effect is like a discrete state at the band edge superimposed on a smooth varying continuum below the edge. This density of states peak at E_0 is responsible for the two-level anticrossing behavior.

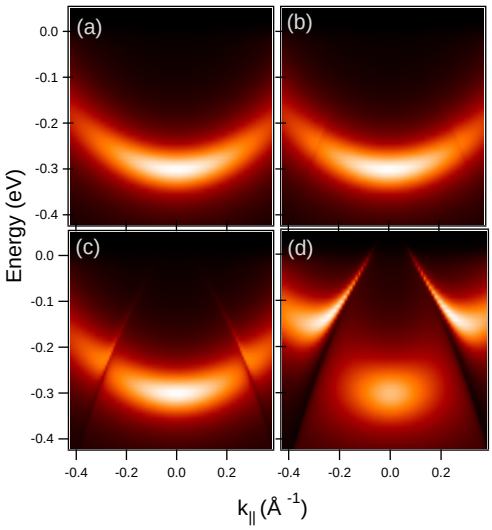

Figure 4.12: The simulation about the substrate effect of the QWS dispersion(a)No interaction (b)HH band edge interaction V equals to 0.0001 (c) V=0.001 (d) V=0.01 .

To understand clearly, we use this model to do simple simulation for the interaction between the substrate and Pb films. Assume a quantum well state with binding energy at -0.3 eV at zone center and only the HH band edge existed interaction with the films, if there is no interaction between the HH band edge and the QWS, the band dispersion is approximately parabolic as shown in Fig. 4.12(a). Fig. 4.12(b)(c)(d) exhibit the change of the QWS dispersion with the increasing interaction potential. The dispersion of QWS exhibits a break as they cross the band edge and the distortion of the band is more evident with stronger interaction, as shown in Fig. 4.12(d).

Therefore, the other affecting factor is the coupling matrix element between the substrate states and the quantum well states. If there is no interaction between the substrate and the film, the spectral function will be a Lorenzian function only for quantum well states and there won't be any break as QWS cross the band edge. In

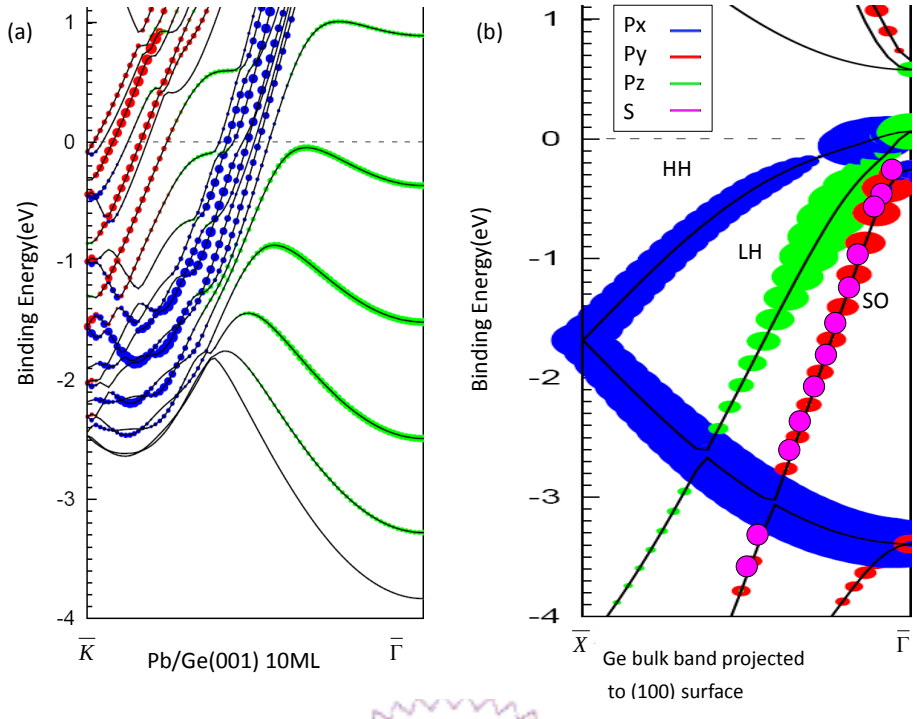

Figure 4.13: (a) Calculated QWS band structure of 10ML Pb film along $\overline{\Gamma K}$ direction (b) Calculated projected band edge of Ge(001) surface. Each color indicates different atom orbital symmetry: blue is P_x, red is P_y, green is P_z and pink is S.

Fig. 4.11, we just find the breaks occur near the LH and SO band edges, but no break occurs in the HH band edge. So we speculate the coupling matrix element between the heavy hole and the Pb QWS subband is zero. The coupling matrix element can be expressed explicitly as

$$< \Psi_{QWS}(S, P_x, P_y, P_z)|V_{interact}(x, y, z)|\Phi_{substrate}(S, P_x, P_y, P_z) > \qquad (4.2)$$

To explain the result, we perform the first-principles calculation of discrete Pb subbands and Ge bulk bands projected to (001) surface, as shown in Fig. 4.13. And then we identify the orbital symmetry of each band. QWS subbands of Pb contain P_z symmetry near the surface zone center $\overline{\Gamma}$. HH band exhibits P_x symmetry. LH band exhibits P_z symmetry, and SO band has the mixture of P_y and S symmetry.

Furthermore, we can use the wave functions of the stationary states of an electon in a spherical symmetric field as below [5]:

$$\psi_{nlm}(r,\theta,\phi) = R_{nl}(r)Y_{lm}(\theta,\phi)$$

where $R_{nl}(r)$ is the radial wave function, depending on the principle quantum number n and the orbital quantum number l. $Y_{lm}(\theta,\phi)$ is the spherical harmonics, depending on l and the magnetic quantum number m.

for s state (l=m=0):

$$\psi_{n00} = R_{n0}(r)$$

for p state (l=1):

$$\psi_{n10} = R_{n1}(r)(3/4\pi)^{1/2}\cos\theta$$

$$\psi_{n11} = R_{n1}(r)(3/8\pi)^{1/2}\sin\theta e^{i\phi}$$

$$\psi_{n1,-1} = R_{n1}(r)(3/8\pi)^{1/2}\sin\theta e^{-i\phi}$$

Any linear combination of these functions will also give the wave function of a p-state as the following equation.

$$\psi_x = 1/\sqrt{2}(\psi_{n11} + \psi_{n1,-1}) = r\sin\theta\cos\phi\cdot f(r)$$

$$\psi_y = 1/\sqrt{2}(\psi_{n11} - \psi_{n1,-1}) = r\sin\theta\sin\phi\cdot f(r)$$

$$\psi_z = \psi_{n10}(r) = r\cos\theta\cdot f(r)$$

where $f(r)$ is the radial wave function, which is determined by the potential energy of an electron moving in the field of an isolated atom. Moreover, we can approximately consider the interaction potential as isotropic in the direction the surface plane, i.e. xy plane, as implied from the LEED pattern of Pb films as shown in Fig. 4.14. Due to this isotropic symmetry in the (111) plane, the integration of the azimuthal part would be zero if either of the wavefunctions of Pb QWS and Ge bulk band edges don't have the variable of azimuthal angle ϕ, as manifested by Eq. (4.2). Therefore, the Eq.(4.2) can be rewritten as for HH band :

$$< \Psi_{QWS}(P_z)|V_{interact}(z)|\Phi_{substrate}(P_x) >= 0$$

By examing the orbital symmetries of Pb QWS and Ge band edges, the coupling matrix element between QWS with P_z symmetry and the HH bulk band edge with the P_x symmetry would fit the scenario, hence causing the matrix element of the interaction potential to be zero. This symmetry argument can therefore explain why the QWS subbands don't interact with Ge HH band edge, as we observed.

4.3.2 Layer Resolution

As mentioned above, the QWS peaks are sharp in the band gap above the projected bulk band of Ge. Below the band edge, the QWS become QWR with much broader linewidths due to degenerate coupling to the substrate states. QWS lineshape reflecting atomic-layer resolution is therefore most evident within the Ge gap, and the gap region is more accessible at the region far from zone center. Thus, we can identify each band with corresponding integer layers clearly at off-normal emis-

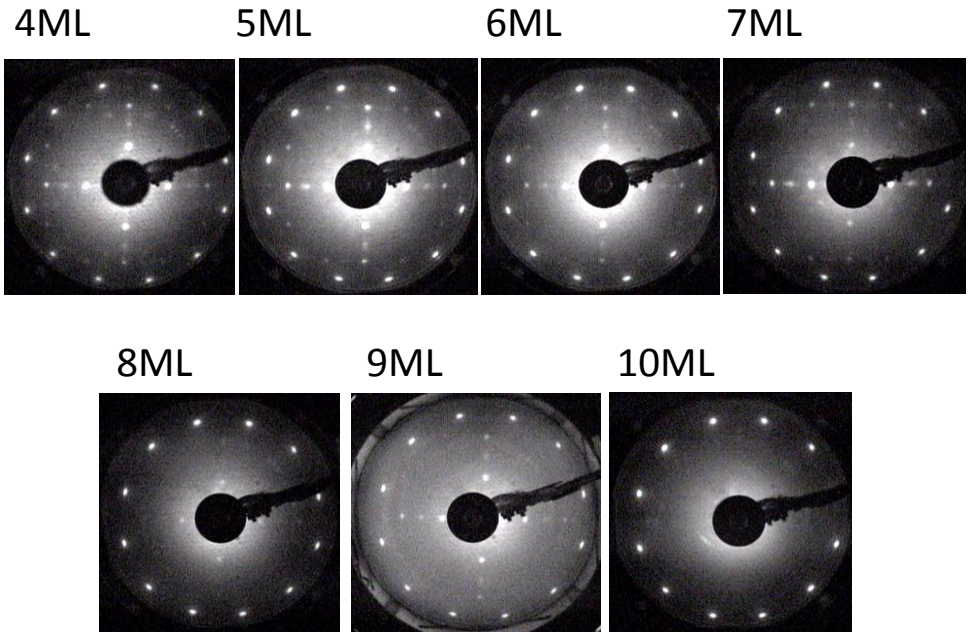

Figure 4.14: LEED patterns of different integer layers at 40eV.

sion in the photoemission. In Fig. 4.10, we illustrate Pb subbands corresponding to different integer layers with different colors : blue and red curves indicate the subbands of the corresponding N layers, green represents the N+1 layers and light blue indicates the N-1 layers. As seen, for most of odd layers, only the subbands corresponding to N layers exist, but for even layers, both subbands, corresponding to N-1 and N+1 layers coexist. Specially we find that the band splitting occurs above the band edge at off-normal position in the photoemission image of even layers, as shown in Fig. 4.15. We superimposed the calculated Pb subbands onto the photoemission data and find that the band splitting is due to the presence of two thicknesses, the N+1 and the N-1 monolayers, in the films for even layers. To confirm the result, we deposited Pb film at the intermediate thickness between 7ML and 8ML, and we find that there is only one subband corresponding to 7ML in the off-normal gap region, as indicated by the circle in Fig. 4.16(a). On the contrary, when the thickness is

in between 8 and 9ML, only one subband corresponding to 9ML is present in the off-normal gap region; as indicated by the circle in Fig. 4.16(c). In Fig. 4.16(b) where Pb film is at the thickness of 8ML, two subbands corresponding to 7 and 9ML, respectively are observed to coexist.

Further we choose the EDCs at off-normal position to investigate the evolution of line shape with thickness. As shown in Fig. 4.17, the peaks corresponding to 7ML and 9ML coexist as the peak of 8ML reach the maximum intensity. Thus, we can conclude that each film of even layers, such as 6ML, 8ML and 10ML, not only consists of itself but also the N+1 and the N-1 layers. This implies the films of even layers are unstable. This is consistent with the results from the thermal stability measurement. Fig. 4.18 exhibits the measured stability temperatures at various thicknesses of Pb film on Ge(001). The stability temperature of even layers is lower than odd layers, indicating the films of odd layers are more stable than even layers.

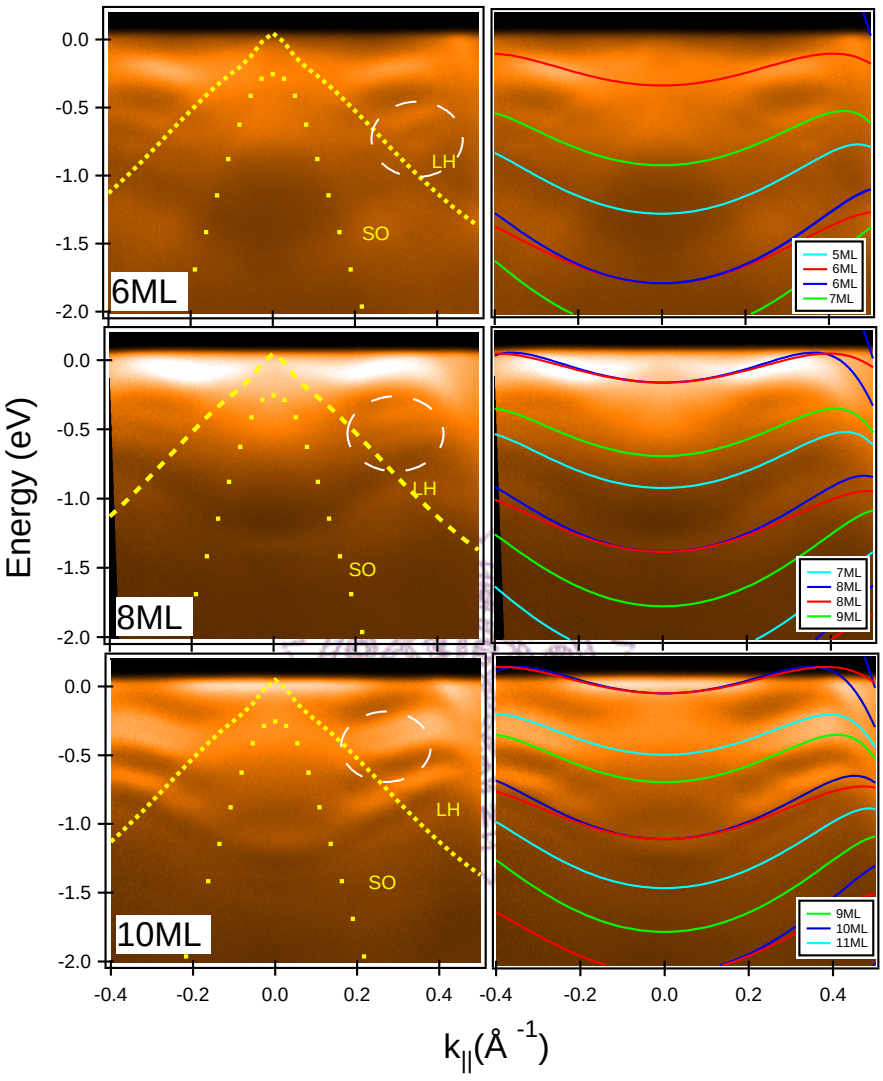

Figure 4.15: The left panel presents the photoemission spectrum for 6, 8 and 10ML of Pb/Ge(001) and the circles exhibit the band splitting. And the right panel shows the calculated Pb subbands which are superimposed onto the data. These splitting bands correspond to the linear combination of Pb subbands which belong to the previous and the next layers for even integer layers itself and appear within the white circles.

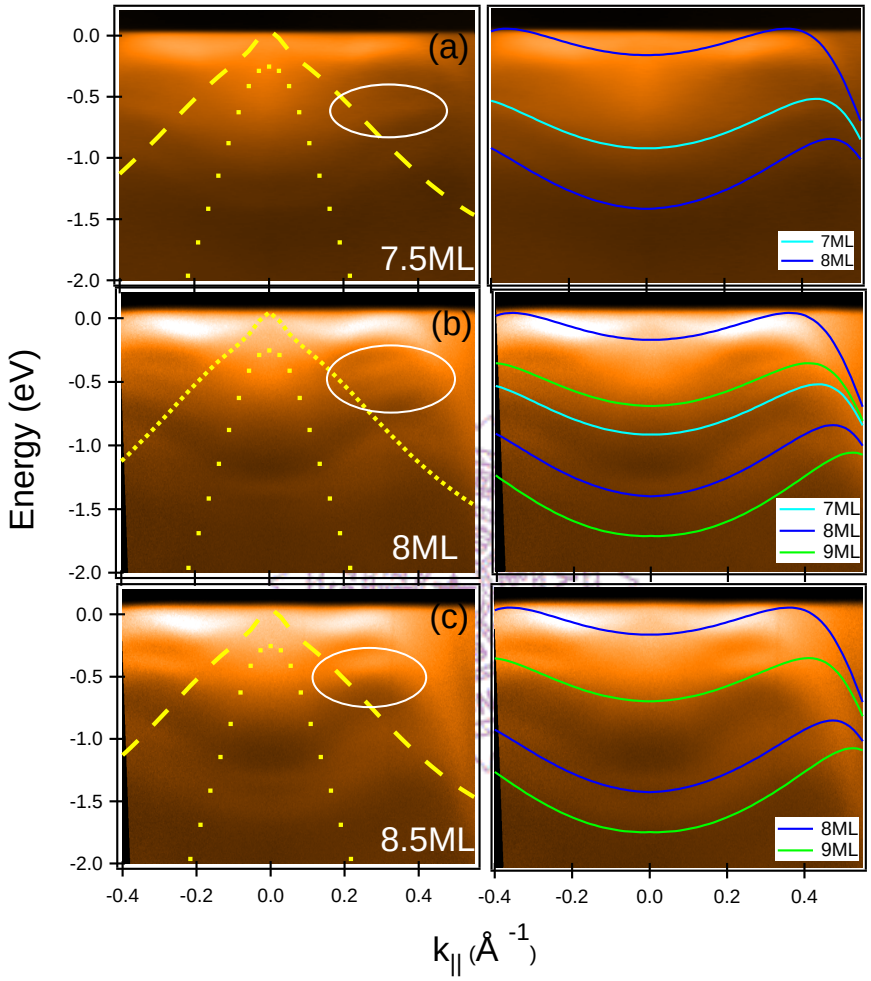

Figure 4.16: Angle-resolved photoemission data presented the band dispersions for (a)about 7.5ML, (b)8ML, and (c)about 8.5ML of Pb on Ge(001). The two concave curves represent projected bulk band edges in Ge.

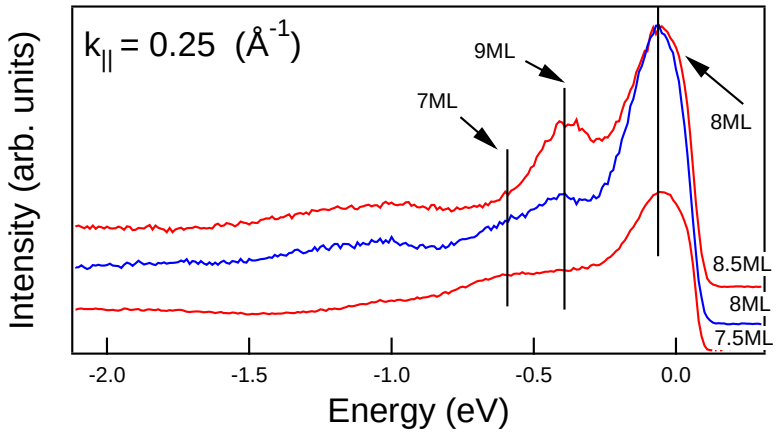

Figure 4.17: The energy distribution curves of 7.5ML, 8ML and 8.5ML at off-normal emission angle 8 degree. The arrows indicate the peaks corresponding to 7ML, 8ML and 9ML.

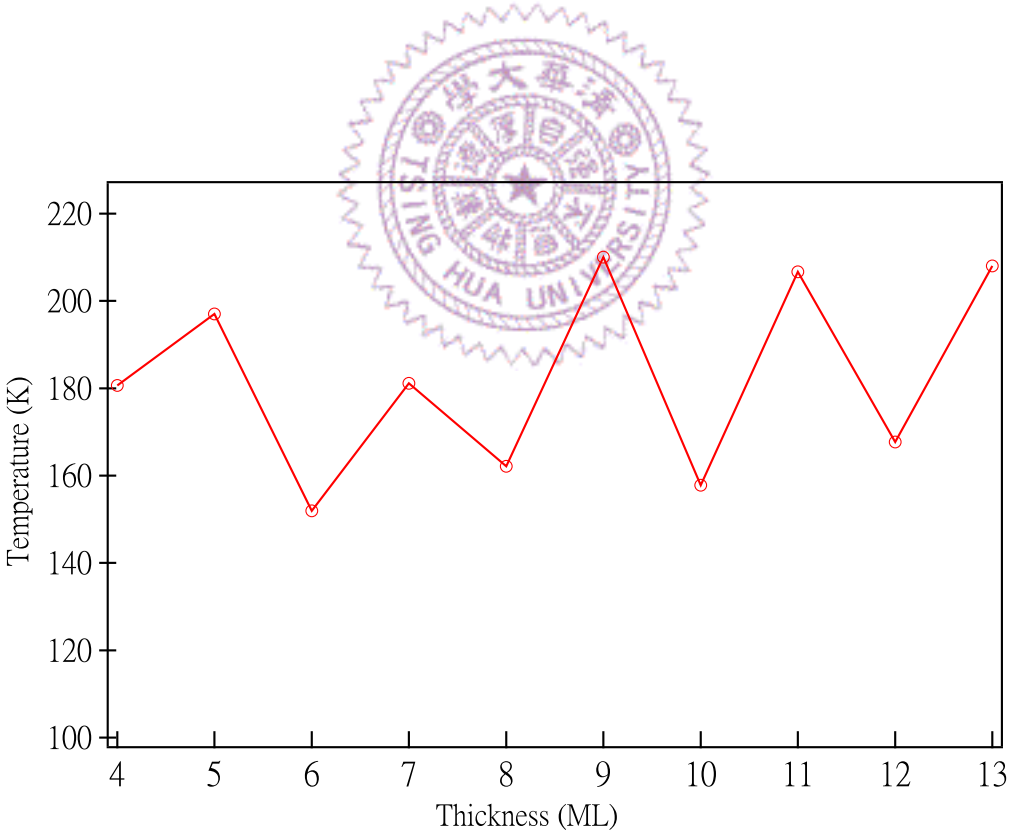

Figure 4.18: Annealing temperature as a function of thickness at which Pb films grown on Ge(001).

Chapter 5

Conclusion

This thesis has presented the research about the properties of thin Pb films deposited on Pb-$c(4\times8)$ Ge(001) reconstructed surface. These properties were probed experimentally with angle-resolved photoemission spectroscopy and the data were analyzed and interpreted in the context of theoretical models.

Overlayer Pb films can grow layer-by-layer on Pb/Ge(001)-c(4 × 8) phase and the films were successfully prepared at the thicknesses ranging 4∼16 monolayers. The measurement of the thickness dependence of the in-plane band dispersions of QWS for Pb films on Ge(001) was performed and the peak positions of QWS were analyzed by Bohr-Sommerfeld quantization rule. According to these discrete peak positions of QWSs, we calculate the Pb bulk subbands to simulate the quantum well states by using Tight-binding approximations. The band dispersions measured by ARPES match the calculated Pb bulk subbands well at off-normal emission except for those near normal emission, where QWS are actually resonances with broad linewidths and interacting with LH and SO Ge band edges. Thus, we can identify

each band with corresponding integer layers clearly at off-normal emission.

From the comparison between the measured and calculated bands, we find some interesting points as bellow:

- Above the LH band edge, the QWS peaks become much sharper and thus reveal layer resolution.
- Due to the isotropic symmetry of the two-domains Pb(111)films on Ge(001), there is no interaction between the HH band and the QWS of Pb film.
- The band splitting occuring near the LH band edge for even layers is caused by the presence of two thicknesses, the N-1 and the N+1 layers.
- The films of odd layers are more stable than even layers.

Furthermore, we can calculate the surface energy to confirm the result of film stability with various thickness or investigate the atomic structure of film thickness for even layers by STM . And Pb films deposited on Si(001) should be studied in the future for comparison.

Bibliography

[1] Stefan Hüfner, *Photoelectron Spectroscopy*, Springer

[2] Hans Lüth, *Surfaces and Interfaces of Solid Materials* , Springer

[3] G. Ertl , J. Küppers, *Low Energy Electrons and Surface Chemistry*, VCH, Weinheim (1985)

[4] Holger T. Grahn *Introduction to semiconductor physics* World Scientific

[5] Sydney G. Davison and Maria Steślicka *Basic Theory of Surface States* Clarendon Press · Oxford (1992)

[6] Andrea Damascelli *Probing the electronic structure of complex systems by ARPES* Physica Scripta Vol.T109,61-74 (2004)

[7] P. E. J. Eriksson, M. Adell, Kazuyuki Sakamoto, and R. I. G. Uhrberg, *Phys. Rev. B* ***77****, 085406* (2008)

[8] T.-C. Chiang *Photoemission studies of quantum well states in thin films*(2000)

[9] *http://www.nsrrc.org.tw/english/lightsource.aspx* , NSRRC

[10] *User Manual SCIENTA R3000* , VG SCIENTA

[11] Peter Y. Yu and Manuel Cardona, *Fundamentals of Semiconductors*, Springer

[12] *http://cst-www.nrl.navy.mil/bind/static/index.html*

[13] Dominic A.ricci , *Photoemission Studies of Interface effects on thin film properties* PhD thesism , University of Illinois at Urbana-Champaign(2006)

[14] E.W.Plummer and W.Eberhardt *Angled-Resolved photoemission As Tool for the study of surfaces*

[15] J. J. Paggel, T. Miller, and T.-C. Chiang *Phys. Rev. Lett.* ***81****, 5632V5635* (1998)

[16] N. W. Ashcroft and D. N. Mermin.G. Ertl , J. Küppers, *Solid State Physics*, Saunders College Publishing (1976).

[17] S. D.Kevan, *Phys. Rev. B* ***32****, 2344* (1985)

[18] Iwao Matsuda and Toshiaki Ohta, *Phys. Rev. B* ***65****, 085327* (2002)

[19] S.-J. Tang, Tay-Rong Chang, Chien-Chung Huang, Chang-Yeh Lee, Cheng-Maw Cheng, Ku-Ding Tsuei, H.-T. Jeng, and Chung-Yu Mou, *Phys. Rev. B* ***81****, 245406* (2010)

[20] M. H. Upton, T. Miller, and T. C. chiang, *Phys. Rev. B.* ***71****, 033403* (2005)

[21] A. Mascaraque, J. Avila, J. Alvarez, M. C. Asensio, S. Ferrer, and E. G. Michel, *Phys. Rev. Lett.* ***82****, 2524* (1999)

[22] G. Falkenberg, L. Seehofer, R.L. Jonson and R. Rettig, *Surface Science* ***372****, 155* (1997)

[23] Yang Guo, Yan-Feng Zhang, Xin-Yu Bao, Tie-Zhu Han, Zhe Tang, Li-Xin Zhang, Wen-Guang Zhu, E. G. Wang, Qian Niu, Z. Q. Qiu, Jin-Feng Jia, Zhong-Xian Zhao, and Qi-Kun Xue, *Science, December 306, 1915-1917*(2004)

[24] D.-A. Luh, T. Miller, J. J. Paggel, and T.-C. Chiang, *Phys. Rev. Lett. textit*88*, 256802*(2002)

[25] A.Crottni, D.Cvetko, l.Floreano, R. Gotter, A.Morgante, and F.Tommasini, *Phys. Rev. Lett.* ***79****, 1527* (1997)

[26] D.Cvetko, A.Verdini, G.bavdek, F.Bruno, A.Cossaro, L.Floreano, A.Morgante *Surface Science and Nanostructures,Reasearch Highlights*

[27] Yun Zhang, R.g. Zhao and W.S. Yang, *Surface Science Letters,* ***293****, L821-L825*(1993)

[28] S.-J.Tang, L.Basile, T.Miller, and T.-C. chiang, *Phys. Rev. B.* ***93****, 216804*(2004)

[29] P.W. Anderson, *Phys. Rev.* ***124****, 41* (1961)

[30] D.M. Newns, *Phys. Rev.* ***178****, 1123*(1969)

[31] C. M. Wei and M. Y. Chou, *Phys. Rev. B.* ***66****, 233408* (2002)